Redox-dependent condensation and cytoplasmic granulation by human ssDNA binding protein 1 delineate roles in oxidative stress response

Gábor M. Harami[1,2,†], János Pálinkás[1,†], Zoltán J. Kovács[1,3,†], Krisztián Tárnok[4], Hajnalka Harami-Papp[1,2], József Hegedüs[1], Lamiya Mahmudova[1], Nóra Kucsma[5], Szilárd Tóth[5], Gergely Szakács[5], Mihály Kovács[1,3,*]

[1] ELTE-MTA "Momentum" Motor Enzymology Research Group, Department of Biochemistry, Eötvös Loránd University, Pázmány P. s. 1/c, H-1117 Budapest, Hungary
[2] Present address: Laboratory of Single Molecule Biophysics, National Heart, Lung and Blood Institute, National Institutes of Health, Bethesda, Maryland 20892, USA
[3] ELKH-ELTE Motor Pharmacology Research Group, Department of Biochemistry, Eötvös Loránd University, Pázmány P. s. 1/c, H-1117 Budapest, Hungary
[4] Department of Physiology and Neurobiology, Eötvös Loránd University, Pázmány P. s. 1/c, H-1117 Budapest, Hungary
[5] Institute of Enzymology, Research Centre for Natural Sciences, Hungarian Academy of Sciences, Magyar Tudósok körútja 2, H-1117 Budapest, Hungary
† Authors contributed equally.
* Corresponding author. Email: mihaly.kovacs@ttk.elte.hu

ABSTRACT

Human single-stranded DNA binding protein 1 (hSSB1/NABP2/OBFC2B) plays central roles in the repair of DNA breaks and oxidized DNA lesions. Here we show that hSSB1 undergoes liquid-liquid phase separation (LLPS) that is redox-dependent and requires the presence of single-stranded DNA or RNA, features that are distinct from those of LLPS by bacterial SSB. hSSB1 nucleoprotein droplets form under physiological ionic conditions, in response to treatment resembling cellular oxidative stress. hSSB1's intrinsically disordered region (IDR) is indispensable for LLPS, whereas all three cysteine residues of the oligonucleotide/oligosaccharide-binding (OB) fold are necessary to maintain redox-sensitive droplet formation. Proteins interacting with hSSB1 show selective enrichment inside hSSB1 droplets, suggesting tight content control and recruitment functions for the condensates. While these features appear instrumental for genome repair, we also detected hSSB1 condensates in the cytoplasm in response to oxidative stress. hSSB1 condensates colocalize with stress granules, implying unexplored extranuclear roles. Our results suggest novel, condensation-linked roles for hSSB1 linking genome repair and cytoplasmic defense.

INTRODUCTION

Single stranded (ss) DNA binding (SSB) proteins are found in all living organisms (*1*). Their main function is the binding and stabilization of exposed ssDNA regions that form during DNA metabolic processes including replication, recombination, and repair (*2*). Protection of ssDNA regions from nucleolytic cleavage, unproductive secondary structure formation and harmful chemical alterations is essential for genome integrity. Moreover, SSBs specifically interact with several other proteins participating in genome maintenance, conferring an organizing hub function for SSBs in DNA metabolism (*1*, *3*). A 19-kDa subunit of the "prototypic" homotetrameric SSB of *Escherichia coli* (EcSSB) comprises an N-terminal oligonucleotide/oligosaccharide binding (OB) fold followed by an intrinsically disordered region (IDR) (*4*) (**Fig. 1A**). Besides mitochondrial SSB, the heterotrimeric replication protein A (RPA) was considered as the only functional metazoan SSB until the discovery of SSB homologs SSB1 and SSB2 (termed hSSB1/NABP2/OBFC2B and hSSB2/NABP1/OBFC2A, respectively, in humans) (*5*). hSSB1 and hSSB2 share high structural similarity to EcSSB, having an N-terminal OB fold followed by C-terminal IDR (**Fig. 1A-B**) (*4*, *6*). hSSB1 is expressed ubiquitously in human tissues, while hSSB2 expression is restricted mainly to immune cells and testes (*7*). Growing evidence highlights central functions for hSSB1 in DNA repair (*8*), telomere maintenance (*9*), RNA transcription (*10*), and embryonic development (*11*). While hSSB1 appears to perform wide-ranging cellular functions, most of our knowledge comes from studies focusing on its DNA repair function. hSSB1 was shown to be an early sensor of DNA damage upon ionizing radiation (IR), whereby it localizes to DNA double strand break (DSB) repair foci and organizes subsequent homologous recombination (HR) mediated DNA repair (*5*, *12*). hSSB1 facilitates DNA end resection, an early step in HR, by recruiting the MRN complex (*13*) and stimulating Exo1 activity (*14*). D-loop formation by RAD51 recombinase, a key step in early HR, is also facilitated by hSSB1 (*5*). hSSB1 colocalizes with Bloom's syndrome helicase (BLM) on IR-induced DSBs (*15*). While hSSB1 is dispensable for normal S-phase DNA replication, it is required for stabilization and restart of replication forks that collapsed upon hydroxyurea treatment (*16*). Another major role of hSSB1 is exerted during the repair of oxidative DNA damage (such as formation of 8-oxoguanine) via the hOGG1-mediated base excision repair

(BER) pathway. hSSB1 relocalizes to chromatin after H_2O_2-induced oxidative stress to recruit hOGG1 to sites of damage and to stimulate its incision activity (*8*).

While EcSSB is a stable homotetramer, the ability of hSSB proteins to self-oligomerize appears more dynamic and is of functional significance. Under reducing conditions, hSSB1 was shown to be dominantly monomeric (*6*, *17*). However, unlike EcSSB that lacks cysteines, hSSB1 contains three conserved cysteine residues (at amino acid (aa) positions 41, 81, and 99; **Fig. 1B**) that could potentially facilitate redox-dependent covalent oligomerization via disulfide bonds. hSSB1 was indeed shown to oligomerize covalently upon oxidative stress, with this feature being abolished by the C99S or C41S substitutions (*17*). Based on the observed oligomerization propensity and tetrameric structure of other SSBs, Touma et al. proposed a structural model in which the hSSB1 tetramer is stabilized by C81-C81 and C99-C99 disulfide bridges, whereas C41 buried inside the OB fold may act as a redox sensor, with its oxidative status allosterically influencing protein structure (*18*). Although the structures of hSSB1 oligomeric forms have not been experimentally clarified, oxidation-dependent hSSB1 oligomerization was found necessary for efficient hOGG1-mediated BER and also for enhanced hSSB1 binding to DNA containing oxidative lesions (*8*), but appears dispensable for DSB repair (*17*). Furthermore, hSSB1 was observed as a monomer in the ternary SOSS (sensor of ssDNA) complex formed with Integrator complex subunit 3 (INTS3) and SOSS complex subunit C (INIP, C9Orf80, hSSBIP1) proteins (*19*, *20*). hSSB1 directly interacts with INTS3, and the complex plays an essential role in HR-mediated DSB repair via ATM activation, RAD51 recruitment to DNA damage (*20–22*), and facilitation of DSB resection by Exo1 (*14*). However, hSSB1 oligomerization proposedly does not interfere with INTS3 interaction (*18*). Taken together, these data point to the functional importance of various homo- and heterooligomeric forms of hSSB1 in oxidative stress response.

We recently discovered that EcSSB forms liquid-like dynamic condensates under physiological conditions *via* liquid-liquid phase separation (LLPS) (*23*). SSB-interacting proteins are selectively enriched inside droplets, while droplet formation is inhibited by ssDNA. Together with earlier data on subcellular distribution of EcSSB (*24*), these findings led to a model in which EcSSB condensates serve as organizers of bacterial genome maintenance (*23*). Upon genomic stress resulting in exposed ssDNA, droplet contents (EcSSB and partner proteins) can be rapidly deployed at the site of action. In this work we also raised the possibility of hSSB1 (and hSSB2) condensation based on *in silico* predictions (*23*).

Here we show that hSSB1 indeed forms LLPS condensates, with properties that markedly differ from those of bacterial SSB. hSSB1 droplet formation requires coacervation with nucleic acids and is tightly regulated by redox conditions, suggesting the importance of LLPS upon oxidative stress, e.g., in the repair of oxidative DNA lesions and/or in stress-related transcription regulation. Covalent oligomerization is not a prerequisite for hSSB1 LLPS; however, all hSSB1 cysteines are necessary for redox-dependent condensation. Furthermore, cytoplasmic hSSB1 droplets were also observed in cell culture in response to oxidative stress, colocalizing with stress granules, pointing to unexplored extranuclear stress response roles for hSSB1. These results extend the emerging concept of nucleoprotein LLPS centrally contributing to genome maintenance and other areas of cellular stress response.

RESULTS

hSSB1-ssDNA and hSSB1-ssRNA nucleoprotein coacervates form selectively and reversibly under oxidative conditions

Following our previous *in silico* predictions (*23*), epifluorescence microscopy experiments showed that purified hSSB1 is indeed able to undergo LLPS (**Fig. 2A, fig. S1-2**).

Importantly, however, unlike in the case of EcSSB, where ssDNA inhibited droplet formation (*23*), hSSB1 requires the presence of ssDNA or ssRNA for LLPS. In addition, we found that hSSB1 LLPS requires oxidative conditions (**Fig. 2A**), in line with the established role of the protein in oxidative DNA damage repair (*8*). Hydrogen peroxide (H_2O_2) is a major reactive oxygen species (ROS) *in vivo* (*25*), and it is an established agent to mimic oxidative stress conditions both *in vitro* and in cell culture experiments. Intriguingly, ssRNA induced hSSB1 droplet formation to a limited extent even in reducing conditions; however, LLPS induction by H_2O_2 was apparent even in this case (**Fig. 2A**). We found that hSSB1 binds ssDNA and ssRNA with similar affinities (**Fig. 2B, Table S1**); thus, the different LLPS propensities of the hSSB1-ssDNA and hSSB1-ssRNA nucleoproteins do not result from differences in the strength of protein-nucleic acid interactions. Liquid-like behavior of hSSB1 condensates is supported by spherical morphology and volume-additive fusion of droplets (**Fig. 2C**). In epifluorescence microscopy experiments, condensate formation became apparent at H_2O_2 concentrations in the micromolar range (**Fig. 2D**). Turbidity measurements, which are sensitive to the appearance of small-sized droplets that are yet undetectable in the epifluorescence microscope, indicated phase separation at H_2O_2 concentrations in the low micromolar range, a physiologically relevant regime for cellular oxidative stress (*25*) (**Fig. 2E-F**). Turbidity and microscopy measurements indicated rapid appearance of condensates (< 10 minutes) in response to H_2O_2 treatment, with turbidity eventually decreasing over longer time scales due to droplet fusion, a phenomenon also seen previously with EcSSB (*23*) (**Fig. 2C,E, fig. S3A**). Importantly, EcSSB shows LLPS independent of redox conditions, underscoring the unique nature of redox-sensitive LLPS by hSSB1 (**fig. S3B**). Furthermore, hSSB1 droplet formation was partially reversible upon addition of the reducing agent DTT (**fig. S3C-D**). Prominent droplets disappeared after 1h incubation, leaving only a faint signal on the microscope slide surface. As LLPS systems are generally sensitive to the ionic milieu, we also tested the effect of various salts on hSSB1 LLPS. High, supraphysiological salt concentrations inhibited droplet formation (**fig. S4A-D**), and addition of KCl at supraphysiological concentration rapidly dissolved droplets after 5 seconds (**fig. S5**). Importantly, however, in a phosphate-buffered (pH7.5), quasi-physiological milieu of 140 mM K^+, 10 mM Na^+, 10 mM Cl^-, 8 mM magnesium acetate, and 30 mg/ml PEG_{20000} to mimic crowding, hSSB1 exhibited LLPS in the presence of ssDNA in response to H_2O_2 treatment (**fig. S4E**). Taken together, these findings reflect the propensity of hSSB1 for redox-dependent nucleoprotein coacervate formation under physiological intracellular chemical conditions.

hSSB1 LLPS shows bell-shaped dependence on nucleic acid concentration

In addition to the factors explored above, the total protein concentration and the protein DNA stoichiometry could also influence LLPS behavior. Thus, we investigated the dependency of phase separation on hSSB1 and ssDNA concentrations. Using epifluorescence microscopy, we found that in the presence of a fixed amount of ssDNA, large phase separated droplets started to appear when the bulk hSSB1 concentration reached a threshold around 1 μM (hSSB1 monomer concentrations are stated throughout this article unless otherwise indicated) (**Fig. 3A**). Turbidity measurements also confirmed this observation (**Fig. 3B**). Conversely, using a fixed amount of hSSB1 we found that the formation of phase-separated droplets showed a bell-shaped dependence on nucleic acid concentration (**Fig. 3C**). Maximal induction of phase separation occurred at around 2 μM dT_{79} oligonucleotide concentration, both in microscopy and turbidity experiments (**Fig. 3D**). This corresponds to an ssDNA interaction stoichiometry of around 32 nt (ssDNA nucleotide units)/hSSB1 monomer. This finding may indicate architectural differences between hSSB1 and EcSSB nucleoproteins,

with the latter binding about 35 nt of oligonucleotide by two subunits of a tetramer in LLPS-competent conditions (*23*).

The intrinsically disordered region (IDR) is required for strong nucleic acid binding and LLPS

Previously we found that the IDR of EcSSB is essential for LLPS: IDR-truncated EcSSB showed no LLPS propensity and formed amorphous aggregates (*23*). In addition, the amino acid composition of the EcSSB IDR has also been shown to be an important determinant of LLPS (*26*). Since hSSB1 also contains a long (113-aa) IDR (**Figs. 1, 4A**), and our previous *in silico* analysis predicted high LLPS propensity for this region (*23*), we tested the LLPS propensity of an hSSB1 variant lacking the IDR region (hSSB1-dIDR). We observed no droplet formation for this construct even in the presence of ssDNA and H_2O_2; only aggregates were observed at higher protein concentrations (**Fig. 4A**). We also found that hSSB1-dIDR shows an about 10-fold decrease in ssDNA binding affinity, compared to the wild-type protein (**Fig. 4B, Table S1**); however, hSSB1-dIDR droplets did not form even at quasi-saturating ssDNA concentrations (**fig. S6**). These data demonstrate that the IDR has a moderate contribution to ssDNA binding, but is indispensable for phase separation.

C41 and C99 are required for redox-dependent covalent oligomerization

A possible mechanism underlying the observed redox-sensitive condensation (**Fig. 2A, fig. S3A**) is covalent oligomerization of hSSB1 through (some of) its three conserved cysteine residues (C41, C81, C99) (**Fig. 1B**), which could increase the multivalency of protein-protein and protein-nucleic acid interactions needed for LLPS (*27*, *28*). C41 was shown to be important for redox-dependent covalent oligomerization, but since it is not exposed to solvent, it was hypothesized to allosterically influence the formation of disulfide bridges between C81 and C99 residues *via* its oxidative state (*18*). To determine the contribution of individual hSSB1 cysteines (**Fig. 1B**) to covalent self-oligomerization and LLPS, we generated all possible Cys-to-Ser substitution variants (C41S, C81S, C99S, C41S-C81S, C41S-C99S, C81S-C99S, and C41S-C81S-C99S). We tested the propensity of hSSB1 variants for covalent oligomerization upon H_2O_2 treatment *via* SDS-PAGE densitometry (**Fig. 4C-D, fig. S7**). We found that covalent dimers were the major oligomeric species formed upon oxidation, with discernible appearance of higher-order oligomers in some cases (**fig. S7**). Upon H_2O_2 treatment, about half of the total wild type (WT) hSSB1 pool formed dimers at saturating H_2O_2 concentration (**Fig. 4D, fig. S7B**). C41S and C99S variants showed reduced dimer formation, while C81S retained the WT phenotype. For the C41S-C81S and C41S-C99S double substituted variants, we observed similar inhibition of dimerization to that for C41S and C99S. Interestingly, C81S-C99S rescued the WT phenotype, and its initial distribution in the absence of H_2O_2 showed a higher dimer : monomer ratio than that for WT hSSB1, implying that the combined absence of C81 and C99 thiols rendered C41 capable of disulfide formation (**fig. S7B**). As expected, the triple substituted variant C41S-C81S-C99S showed no covalent oligomerization. Taken together, these data show that both C41 and C99, but not C81, crucially contribute to redox-dependent covalent dimerization.

All cysteines of hSSB1 are required for redox-regulated LLPS propensity

After asserting that the ssDNA binding properties of the above described hSSB1 variants were not affected by the amino acid substitutions (**fig. S8A, Table S1**), we also investigated the LLPS propensity of these hSSB1 variants (**Fig. 4E**). Interestingly, all constructs retained their ability to undergo LLPS, but the redox sensitivity of this feature was lost in all substituted variants: phase-separated droplets were visible both in the presence of H_2O_2 and in DTT. However, the dependence of droplet formation on the presence of ssDNA

was unaffected; variants were unable to undergo LLPS in the absence of ssDNA **(fig. S8B)**. With ssDNA present, C41S and C99S, which were less efficient in covalent oligomerization, and even C41S-C81S-C99S showing no covalent oligomerization, were still able to form phase-separated droplets. These findings showed that disulfide formation and covalent oligomerization *per se* are not needed for hSSB1 phase separation, but the presence of all cysteines is needed for redox-sensitive behavior.

Genome maintenance proteins are selectively enriched in hSSB1 droplets that act as molecular filters

hSSB1 was shown to promote recruitment of Bloom's syndrome (BLM) helicase to double-stranded DNA breaks during HR (*15*). In addition, integrator subunit 3 (INTS3) is a major interacting partner of hSSB1 (and hSSB2) in the ternary SOSS complex, which is crucial for DSB repair (*20–22*) **(Fig. 5A)**. Our fluorescence microscopy experiments showed that the mentioned proteins, and also hSSB2, were readily enriched inside LLPS droplets formed by hSSB1 **(Fig. 5B-C)**. The SOSS component INIP, which only forms interactions with INTS3 but not with hSSB1 (*20*), showed enrichment in hSSB1 droplets only in the presence of INTS3 **(Fig. 5B-C)**. In the lack of specific interactions, with hSSB1, neither the protein EGFP nor the small molecule fluorescein become enriched in condensates **(Fig. 5B-C)**, indicating strong regulation regarding the contents of hSSB1 LLPS droplets. These data show that hSSB1 condensates exert molecular filter functions by selectively recruiting and retaining interaction partners, similar to what we observed for the EcSSB protein (*23*).

Significant fraction of hSSB1 localizes to the cytoplasm

Upon our *in vitro* observation of redox-sensitive LLPS by hSSB1 in the presence of either ssDNA or ssRNA, we sought to explore the possibility of intracellular condensation of endogenous hSSB1 in HeLa cells under oxidative stress. Albeit hSSB1 has previously been implicated in nuclear functions, we detected its presence throughout the cell, both in the nucleus and cytoplasm, with the exception of the nucleolus (**Fig. 6A**). In untreated cells, the majority of hSSB1 is found in the nucleus, but a discernible fraction is located in the cytoplasm (**Fig. 6A**). Under these conditions, the cytoplasmic hSSB1 fraction showed disperse distribution with no apparent local enrichment or condensation. Paquet *et al.* detected hSSB1 recruitment to chromatin upon oxidative stress in U2OS cells (*8*). We did not observe a similar phenomenon in HeLa cells, as even untreated cells showed strong nuclear localization of hSSB1 whose pattern did not change upon H_2O_2 treatment (**Fig. 6A**); even a small decrease in nuclear hSSB1 fluorescence intensity was seen upon 1 mM H_2O_2 treatment in immunocytochemical experiments (**Fig. 6B**). These data show that a discernible fraction of hSSB1 is present in the cytoplasm.

Acute oxidative stress induces hSSB1 organization into cytoplasmic foci that colocalize with stress granules

Using immunostaining, we observed that, upon acute oxidative stress caused by H_2O_2 treatment, endogenous hSSB1 became organized in multiple dense cytoplasmic foci in the size range of < 1 µm (**Fig. 6A**). Our *in vitro* measurements confirmed the ability of the applied antibodies to enter and stain hSSB1 droplets, thus enabling immunostaining of hSSB1 under LLPS conditions (**fig. S9**). Stress granules (SGs) have been identified as cytoplasmic, membraneless ribonucleoprotein granules that form upon rapid changes in intra- or extracellular conditions, including oxidative stress (*29, 30*). SGs exhibit liquid-like properties and were implicated in fine-tuning protein expression to adapt to changed environments. Ras GTPase-activating protein-binding protein 1 (G3BP1) was shown to be a major factor for SG assembly (*31*); therefore, we used G3BP1 staining to visualize SGs and assess their

colocalization with hSSB1 granules. Diffuse G3BP1 staining with no SG formation was observed in untreated cells (**Fig. 6A**). However, we were able to trigger SG formation upon acute H_2O_2 treatment (**fig. S10**) and observed strong colocalization between cytoplasmic hSSB1 granules and SGs (**Fig. 6C-D**).

We also assessed hSSB1 subcellular patterns by transiently overexpressing EGFP-fused hSSB1 (hSSB1-EGFP) in HeLa cells. Interestingly, cells overexpressing hSSB1-EGFP showed granulation of both hSSB1-EGFP and G3BP1 even in the absence of oxidative stress, which was not seen in non-transfected cells (**fig. S11A, cf. Fig. 6A**). Therefore, we investigated whether overexpression of hSSB1-EGFP, or that of EGFP alone, can induce SG formation. Assessed as a function of H_2O_2 concentration, we found the fraction of SG-containing cells to be similar in both EGFP- and hSSB1-EGFP expressing cells, with hSSB1-EGFP foci colocalizing with G3BP1 (**fig. S11B-C**). While indicating that the transfection procedure and/or EGFP expression *per se* induce SG formation, in line with recent results suggesting that EGFP expression causes oxidative stress (*32*), these experiments corroborated the inclusion of hSSB1 in stress granules.

hSSB1 granules do not colocalize with P-bodies

Processing-bodies (P-bodies) are membraneless ribonucleoprotein compartments associated with RNA degradation processes and share a number of components with SGs (*33, 34*). However, while microscopically visible SGs are absent under normal conditions, P-bodies are constitutively present and observable at low levels. We used co-staining of P-body marker SK1-Hedls (*35*) and hSSB1 to investigate if hSSB1 droplets colocalize with P-bodies under normal and oxidative stress conditions (**Fig. 7A**). We observed no colocalization between the different condensates, therefore we concluded that hSSB1 is not included in P-bodies (**Fig. 7B**).

DISCUSSION

In this work we show that hSSB1 forms phase-separated liquid condensates under physiologically relevant macromolecular and ionic conditions *in vitro* and forms granules in cells upon acute oxidative stress. hSSB1 coacervates with nucleic acids, both DNA and RNA, in a stoichiometry-dependent fashion, with its condensation being selectively initiated by oxidative conditions (**Fig. 2-3, fig. S3-5**). hSSB1 condensation is effective even at low protein concentrations, without the need for molecular crowders (**Fig. 3A-B**) and is driven by hSSB1's intrinsically disordered region (IDR) (**Fig. 4A, fig. S6**), in line with PDB-deposited crystal structures obtained with a truncated hSSB1 construct supporting the propensity for IDL-IDL intermolecular interactions (PDB codes 5D8E and 5D8F, no accompanying publication) (**Fig. 8A**).

Importantly, the dependence of hSSB1 LLPS on oxidative conditions (**Fig. 2, fig. S3**) strongly suggests a cellular oxidative stress sensing/response role for the protein. Effects caused by ROS are thought to be exerted locally (*36, 37*), where hSSB1 droplets, as first responders, could rapidly form on exposed single-stranded nucleic acid segments.

We also show that other genome maintenance proteins interacting with hSSB1 can readily and selectively be enriched in hSSB1 droplets (**Fig. 5**). hSSB1 condensates can thus recruit required factors to the site of action, and also act as a molecular filter to restrict the localization of other proteins. One such example may be BER where hSSB1 was shown to assist the repair of ROS-induced DNA damage by recruiting hOGG1 to chromatin (*8*). However, considering that we observed hSSB1-driven LLPS also in conjunction with ssRNA (**Fig. 2A**), the roles of hSSB1 LLPS may not be limited to genome repair, as it may also be effective in RNA metabolic processes both in the nucleus and in the cytoplasm (see below).

While intermolecular IDR-IDR interactions appear to be a major driving force for LLPS (**Fig. 4A**), binding of single-stranded nucleic acids is also crucial for coacervation (**Fig. 2A, 3C**). hSSB1 was shown to exist dominantly as a monomer in the absence of nucleic acids (*6, 17*). However, as LLPS processes generally require multivalent interactions, we propose that single-stranded nucleic acids can either act as a scaffold to which multiple hSSB1 monomers can bind sequentially and independently in a beads on a string-like fashion or as a stabilizer for oligomerization (**Fig. 8**). In either case, the multivalency of SSB-SSB interactions is enhanced in addition to the increased local concentration of SSB IDL regions. The bell-shaped ssDNA concentration dependence of hSSB1 LLPS (**Fig. 3C-D**) can be explained based on the beads on a string-like model, regardless of the oligomerization state of the protein. When the concentration of ssDNA molecules exceeds the SSB binding stoichiometry, the probability of multiple SSB molecules binding to the same ssDNA molecule decreases, leading to a lower LLPS propensity. However, our findings that despite significant hSSB1 oligomerization upon oxidation in the absence of nucleic acids, LLPS is only observed upon nucleic acid binding, indicate additional, unexplored roles for nucleic acid binding, potentially distinct from the scaffolding function.

Besides nucleic acid binding, the role of protein oxidation in LLPS regulation is especially intriguing. According to an emerging concept, cysteine residues within proteins may act as regulatory switches in redox signaling (*38, 39*). In this work we comprehensively assessed the roles of each of hSSB1's cysteine residues in the interplay between covalent oligomerization and nucleoprotein condensation (**Fig. 4C-E, fig. S7-8**). On one hand, we show that covalent oligomerization of hSSB1, mediated by residues C41 and C99, is not a prerequisite for forming LLPS condensates (**Fig. 4D**). On the other hand, the capability for covalent oligomerization alone is not sufficient for redox-dependent LLPS, for which all three hSSB1 cysteines are required (**Fig. 4E**). Taken together, our observations point toward a delicate autoregulatory mechanism for LLPS, which apparently involves oxidation-dependent hSSB1 structural changes. While the structure of oxidized hSSB1 is yet unknown, existing crystal structures also support a regulation model as follows. In both of a nucleic acid-free and an ssDNA-bound structure of a truncated hSSB1 construct lacking the majority of the IDR (PDB codes 5D8E and 5D8F), extensive interactions between the remaining C-terminal parts of the tail are observed (**Fig. 8A-B**). In contrast, in the SOSS1 (INTS3, INIP, SSB1) complex, the same region of full-length hSSB1 folds back onto the OB domain both in the presence and absence of ssDNA(*19*). Moreover, the N-terminal part of the IDR is not resolved, probably because it is disordered (**Fig. 8C**). The large difference in protein structure, i.e., the position of the IDR tail, in the above-mentioned structures highlights the mobility of the tail and its capability to either bind to the OB fold intramolecularly or to interact with other hSSB1 tails (**Fig. 8C**). Importantly, in the OB domain-bound form of the IDR, its C-terminal part lies in a valley on the OB domain`s surface, which includes cysteine 81 and a hydrophobic pocket adjacent to C99 (**Fig. 8C**). Based on these observations, we can envision a scenario in which the oxidation of these residues (C81, C99), and also that of cysteine 41, could potentially alter the structure of hSSB1 and significantly weaken the interaction between the IDR and the OB fold. This effect may facilitate intermolecular IDL-IDL interactions that are essential for LLPS. The observed IDR-IDR and IDR-OB interactions are apparently mutually exclusive as they involve the same residues and likely compete with each other based on the structural data.

Our results suggest that all three cysteines in their reduced form contribute to the inhibition of interprotein interactions essential for LLPS, regardless of the presence of nucleic acids, possibly by facilitating IDR-OB fold interactions and thus inhibiting IDR-IDR interactions. Single or combinatorial mutations of any of the cysteines eliminate the inhibitory effect and thus abolish redox sensitivity of hSSB1 LLPS (**Fig. 4E**). In addition, cysteines 99

and 41 are involved in the formation of covalently bound oligomers. While covalent oligomers are not required for hSSB1 LLPS, they were shown to bind ssDNA with enhanced affinity compared to the monomeric form, indicating a role in regulating interactions within and stability of the nucleoprotein complex (*40*). In addition, disulfide bridges may stabilize the IDR in an OB-unbound form in hSSB1 oligomers. Based on the above findings, we propose a model for a regulatory mechanism that ensures that robust LLPS is only triggered when the hSSB1 protein is oxidized and bound to nucleic acids (**Fig. 8D**). Although redox-dependent regulative modifications are being identified in an increasing number of proteins (*41*), evidence is still scarce for redox-sensitive amino acid modifications governing LLPS propensity. Examples include disulfide formation-dependent LLPS by TMF (terminating flower) transcription factor, governing plant tissue development in the apical meristem (*42*), and LLPS by yeast Ataxin-2 mediated by reversible oxidation of methionine (*43*). Further exploration of redox-dependent molecular changes in hSSB1 nucleoprotein coacervates will likely yield key insights into mechanisms of oxidative stress response.

In addition to our biochemical results, we found that a discernible fraction of the hSSB1 protein is present in the cytoplasm, which is organized into distinct granules upon acute oxidative stress (**Fig. 6A-B**), although this far only nuclear functions have been described for hSSB1. Cytoplasmic hSSB1 foci colocalize with stress granules (**Fig. 6C-D**) but not with P-bodies (**Fig. 7**). Interestingly, hSSB1 has not been implicated to be me a member of the SG proteome by previous approaches aiming to identify SG constituents (*44*).

The previously reported increased H_2O_2 sensitivity of cells upon hSSB1 silencing was interpreted as a result of the defect in the repair of 8-oxoguanine DNA lesions through BER (*8*). However, our current findings suggest that hSSB1 plays additional roles in processes distinct from genome repair. We find that hSSB1 forms coacervates with ssRNA as effectively as with ssDNA (**Fig. 2A**). Thus, ssDNA regions appearing upon DNA damage can act as a scaffold to initiate hSSB1-driven LLPS in the nucleus, while in the cytoplasm ssRNA regions can facilitate droplet formation and incorporation of hSSB1 condensates into SGs. Further exploration of the cytoplasmic functions of hSSB1 is required to reveal its potential roles in SG processing, content control, and disassembly.

The potential role of hSSB1 and its discovered LLPS propensity in oxidative stress response is particularly relevant in the context of cancer cells that generally experience chronic oxidative stress. It is plausible that hSSB1's capability to form condensates in a redox-dependent manner supports cancer cell survival. Indeed, hSSB1 is upregulated in a large variety of cancers including gastric and colorectal adenocarcinoma, chronic lymphocytic leukemia, B-cell non-Hodgkin lymphoma, breast adenocarcinoma, and hepatocellular carcinoma (**Fig. 9**). In addition, hSSB1 was recently shown to be involved in DNA damage response and transcription regulation processes in prostate cancer (*45*). Considering that numerous anticancer agents act at least in part by generation of oxidative stress, targeting of hSSB1's LLPS propensity appears as a promising tool to sensitize cancer cells to oxidative stress without compromising the LLPS-independent functions of the protein.

MATERIALS AND METHODS

General reaction conditions

Unless otherwise stated, *in vitro* measurements were performed at 25°C in LLPS buffer containing 25 mM Tris-HCl pH 7.4, 10 mM $MgCl_2$, 50 mM KCl, supplemented with 0.003 % (980 µM) H_2O_2 or 1 mM DTT. LLPS buffer omitting $MgCl_2$ and KCl (denoted as "no salt LLPS buffer") was used where indicated. We note that the latter experiments contained 1.7 mM KCl and 3.4 mM $MgCl_2$ originating from the storage buffer of hSSB1.

Cloning, protein expression and purification

pET29a-hNABP2 (hSSB1), pET29a-hNABP1 (hSSB2), pET28a-C9ORF80, and pGEX-6P-1-INTS3-FL were gifts from Yuliang Wu (Addgene plasmids #128307, 128306, 128418, and 128415, respectively) (*6*, *46*). pET29a-hSSB1 contained a point mutation coding for an Y85C substitution, which was restored to WT tyrosine using QuikChange (Agilent) mutagenesis. QuikChange results were verified by DNA sequencing. Expression and purification of hSSB1 and hSSB2 fused to a C-terminal histidine-tag were performed as described in references (*5*, *6*) with modifications as follows. In the case of hSSB1, Ni-NTA beads were equilibrated with buffer A (25 mM Tris-HCl pH 8.0, 500 mM NaCl, 10 % glycerol, 0.1 % TWEEN 20). Loaded column was washed with 10 column volumes of buffer B (25 mM Tris-HCl pH 8.0, 50 mM NaCl, 10 % glycerol, 0.1 % TWEEN 20) supplemented with 50 mM imidazole. Protein was eluted with buffer B containing 250 mM imidazole, and loaded on HiTrap Heparin column (GE Healthcare) equilibrated with HP1 buffer (25 mM Tris-HCl pH 8.0, 50 mM NaCl, 10 % glycerol). Elution was achieved with HP2 buffer (25 mM Tris-HCl pH 8.0, 1 M NaCl, 10 % glycerol). Purified protein samples were concentrated using Amicon Ultra 10K spin column (Sigma-Aldrich) and dialyzed against Storage buffer (25 mM Tris-HCl pH 8.0, 50 mM KCl, 100 mM $MgCl_2$, 10 % glycerol, 1 mM DTT). Plasmids coding for hSSB1 variants were generated from the Y85C substitution-corrected pET29a-hSSB1 vector using the QuikChange (Agilent) mutagenesis kit, and hSSB1 variant proteins were purified as WT hSSB1. In case of hSSB1-IDR, a stop codon was introduced after the codon coding for aa 109. Mutagenesis was verified by DNA sequencing. In the case of hSSB2, only nickel affinity chromatography was applied.

INTS3 and INIP were purified as described (*46*) with modifications for INTS3 as follows. After sonication, GST-tagged INTS3 was loaded onto Glutathione Agarose (Pierce™) column equilibrated with buffer A (25 mM Tris-HCl pH 8.0, 500 mM NaCl, 1 mM EDTA, 1 mM DTT, 0.2 % Tween 20, 10 % glycerol). Loaded column was washed with 2 column volumes of buffer B (25 mM Tris-HCl pH 8.0, 150 mM NaCl, 1 mM DTT, 0.2 % Tween 20, 10 % glycerol). Precision protease (10 unit/ml) was introduced in buffer B on column and INTS3 was digested overnight. Tag-free protein was eluted with buffer B, then concentrated with Amicon Ultra 100K spin column (Sigma-Aldrich) and dialyzed against Storage buffer (25 mM Tris-HCl pH 8.0, 50 mM NaCl, 10 % glycerol, 1 mM DTT).

Plasmids, expression, and purification of EcSSB, human BLM and EGFP constructs were described in (*23*, *47*).

Purity of samples was checked by tris-glycine based gradient SDS-PAGE (Mini-Protean TGX 4-20 %, Bio-Rad) for all constructs. Bradford method was used for concentration measurement of proteins. Purified proteins were frozen in droplets and stored in liquid N_2.

pEGFP-C1 plasmid, used for transfection of HeLa cells, was obtained from Clontech. The hSSB1 coding sequence was amplified by PCR and cloned upstream of EGFP to fuse hSSB1 to the N-terminus of EGFP. Constructs were verified by DNA sequencing.

Fluorescent labeling of proteins

hSSB2 was labeled with 5-IAF (5-iodoacetamido-fluorescein, Thermo Fisher) on the intrinsic cysteines. hSSB2 Storage buffer (25 mM Tris-HCl pH 8.0, 50 mM NaCl, 100 mM $MgCl_2$, 10% glycerol, 1 mM DTT) was exchanged to a Storage buffer omitting DTT using a PD10 (GE Healthcare) gel filtration column. IAF was applied at 1.5-fold molar excess compared to hSSB2. The labeling reaction was performed for 3.5 h in argon atmosphere, at room temperature. The labeled protein was purified with a PD10 (GE Healthcare) gel filtration column pre-equilibrated with hSSB2 Storage buffer and dialyzed against Storage buffer to remove residual free dye.

INIP was labeled on its N-terminus with AF488 (Alexa Fluor 488 carboxylic acid succinimidyl ester, Thermo Fisher). INIP Storage buffer was exchanged to Labeling buffer (50 mM MES pH 6.5, 50 mM KCl, 10% glycerol) by dialysis. AF488 was introduced in 4-fold molar excess over protein. Labeling process was performed for 5 h at room temperature. Reaction was stopped by 50 mM Tris-HCl final concentration. The labeled protein was purified using a PD10 (GE Healthcare) gel filtration column pre-equilibrated with INIP Storage buffer (25 mM Tris-HCl pH 8, 150 mM KCl, 10% glycerol). INIP was dialyzed against Storage buffer and repetitively filtrated using an Amicon Ultra 10K spin column to remove residual free dye.

hSSB1 and INTS3 proteins were labeled with AF647 (Alexa Fluor 647 carboxylic acid succinimidyl ester, Thermo Fisher). Proteins were dialyzed against Labeling buffer (50 mM MES pH 6.5, 50 mM KCl, 100 mM $MgCl_2$, 5 mM DTT). AF647 was applied at 1.5-fold molar excess over proteins. Labeling reactions were carried out for 3.5 h in the case of both proteins. Reactions were stopped by the addition of 50 mM Tris-HCl final concentration. The labeled proteins were purified with a PD10 (GE Healthcare) gel filtration column pre-equilibrated with Storage buffers (hSSB1: 25 mM Tris-HCl pH 8.0, 50 mM NaCl, 100 mM $MgCl_2$, 10% glycerol, 1 mM DTT; INTS3: 25 mM Tris-HCl pH 8.0, 50 mM NaCl, 10% glycerol, 1 mM DTT). Samples were dialyzed against Storage buffers and in the case of INTS3 an Amicon Ultra 100K spin column (Sigma-Aldrich) was applied to remove residual free dye.

Protein concentrations were determined by Bradford method. Labeling efficiency was determined by visible light spectrometry using $\varepsilon 494 = 80000$ for 5-IAF, $\varepsilon 488 = 73000$ M^{--1} cm^{-1} for AF488, and $\varepsilon 647 = 270000$ M^{--1} cm^{-1} for AF647. Labeling ratios were 60% for hSSB2, 17% for INIP, 10% for hSSB1 and 9.6% for INTS3.

Protein purity was checked for all constructs using SDS-PAGE. All constructs were frozen in liquid N2 in small aliquots and stored at -80 °C. Labeling methods for BLM and EcSSB are described in (*23*).

Fluorescence anisotropy titrations

DNA and RNA binding was measured in FP buffer (25 mM Tris-HCl pH 7.4, 50 mM KCl, 1 mM DTT) with 10 nM of 3'-fluorescein-labeled 36-mer ssDNA or 36-mer ssRNA oligonucleotide (ssDNA: ATTTTTGCGGATGGCTTAGAGCTTAATTGCGCAACG-fluorescein, ssRNA: AUUUUUGCGGAUGGCUUAGAGCUUAAUUGCGCAACG -fluorescein*)*. Fluorescence anisotropy of 12-µl samples was measured in 384-well low-volume nontransparent microplates (Greiner Bio-one, PN:784900) at 25°C in a Synergy H4 Hybrid Multi-Mode Microplate Reader (BioTek) and converted to anisotropy values. Fits were performed using the Hill equation (n = 3 independent measurements).

Turbidity measurements

Turbidity (light depletion at 600-nm wavelength) at indicated hSSB1 concentrations in the presence of 1 µM dT_{79} (79-mer single-stranded deoxythymidine oligonucleotide) was measured in a Tecan Infinite Nano+ plate reader instrument at 25°C. For measurements at low micromolar H_2O_2 concentrations (**Fig. 2E**), DTT was removed from hSSB1 storage buffer using a 10K spin column (Sigma-Aldrich) and DTT concentration was remeasured with DTNB (Ellman's Reagent) to a final concentration of 0.4 µM.

Epifluorescence microscopy for *in vitro* LLPS

A Nikon Eclipse Ti-E TIRF microscope was used in epifluorescence mode with apo TIRF 100x oil immersion objective (numerical aperture (NA) = 1.49). A Cyan 488-nm laser (Coherent), a 543-nm laser (25-LGP-193–230, Melles Griot) and a 642-nm laser

(56RCS/S2799, Melles Griot) were used for excitation. Fluorescence was deflected to a ZT405/488/561/640rpc BS dichroic mirror and recorded by a Zyla sCMOS (ANDOR) camera. Images were captured using the imaging software NIS-Elements AR (Advanced Research) 4.50.00. Experiments were recorded with 2x2 binning and 200-ms laser exposure optical setup. 20-µl volumes of samples were introduced into µ-Slide Angiogenesis (Ibidi) microscope slides at 25°C. Sample components were mixed freshly and incubated for 1 h before imaging, unless indicated otherwise.

In the absence of nucleic acids (**Fig. 2A, fig. S4E, S6, S7B**) and for measurements shown in **Fig. 3C**, 5 µM hSSB1 and 0.1 µM Alexa Fluor 647-labeled hSSB1 ($hSSB1^{AF647}$) were mixed. All nucleic acid-containing experiments were carried out using 5 µM hSSB1 (wild-type or variants) in the presence of 2 µM ssDNA (dT_{79}, containing 100 nM Cy3-labeled dT_{79} or dT_{45}, containing 100 nM Cy3-labeled dT_{45}) or 2 µM ssRNA (U41; 41-mer uridine homopolymer, containing 100 nM Cy3-labeled nonhomopolymeric 41-mer ssRNA) unless indicated otherwise. **Fig. S2** shows that labeled ssDNA can readily enter hSSB1 droplets, thus it can be used for LLPS visualization without the need for protein labeling. For droplet fusion experiment, chambers were treated with 1.5 mg/ml Blocking Reagent (Roche) for 30 min before introducing hSSB1. Fusions were monitored at 4-5 sec intervals.

For multiprotein co-condensation experiments (**Fig. 5**), 180 nM labeled protein interaction partners were used either alone or together with 5 µM hSSB1 containing 0.1 µM AlexaFluor647-hSSB1. Each experiment contained also 2 µM dT_{79} and 980 µM H_2O_2. In the case of labeled hSSB2, BLM, EGFP and fluorescein dye molecules, hSSB1 was incubated for 1 hour before introducing fluorescent partners, then co-incubated with partners for additional 30 min before imaging. Since INTS3 and hSSB1 were both labeled with AlexaFluor647, in experiments containing labeled INTS3, labeled ssDNA (2 µM dT_{79} containing 0.1 µM Cy3-dT_{79}) was used to visualize hSSB1 droplets (5 µM unlabeled protein). Furthermore, in experiments containing INTS3 and/or INIP partners, hSSB1 was co-incubated with partners for 2 hours before imaging. For the INIP + INTS3 complex-containing sample, 180 nM labeled INIP and 1 µM unlabeled INTS3 were used.

Image processing for epifluorescence microscopy

ImageJ software was used to analyze unprocessed images. Image stack was generated from raw images of a given experiment to set brightness and contrast equally, using the automatic detection algorithm. Images were background corrected with the built-in rolling ball background correction, unless otherwise indicated. Montage was generated from stack of a given experiment to visually represent the changing conditions of the experimental set.

Since hSSB1 condensates spread out on the surface of microscope slide over time, instead of droplet size analysis (*23*) we analyzed the mean grey values and total areas of droplets. Stack of 3 images was generated for each condition. Middle ROI (Region of Interest) (area: 600 x 600 pixels; X,Y coordinates from left, uppermost pixel position: 300 pixels) of every stack was selected for technical reasons. Mean grey values (sum of intensity values from all pixels divided by the number of pixels) were measured for each middle ROI using the Stack Fitter plugin, then averaged for each condition separately. For determination of the total droplet area of middle ROIs, background correction thresholds were set using the built-in image thresholder of Fiji. The particle analyzer algorithm of Fiji (smallest detected size was set to 0.2 μm^2, circularity 0.1–1) was applied to outline the distinct fluorescent spot areas of each middle ROI of a stack, which were added together separately and the distinct ROI values of one condition were averaged to get the total droplet area in μm^2.

***In vitro* oxidation experiments**

20 μM of protein was incubated in LLPS buffer for 45 minutes at room temperature with indicated H_2O_2 concentrations. Covalent oligomers were separated via tris-glycine based SDS-PAGE on a 10% polyacrylamide gel. Electrophoresis was performed at 200 V constant voltage for 90 min. Gels were rinsed with ddH_2O and stained overnight with PageBlue Protein Staining Solution (Thermo Fisher) and de-stained in ddH_2O. Fraction of monomers and dimers were analyzed by pixel densitometry using the GelQuant Pro v12 software (DNR Bio Imaging Ltd.).

Cell treatments, transfection

HeLa cells were maintained at 37°C under 5% CO_2 atmosphere in RPMI-1640 medium (ThermoFisher) supplemented with fetal bovine serum, gentamicin and amphotericin B. For transfection, 25,000 cells were seeded onto plasma-sterilized, polylysine-treated coverslips in wells of a 24-well plate. Cells were transfected on the next day with pEGFP-C1 or pEGFP-C1-hSSB1 plasmids, encoding EGFP or EGFP-fused hSSB1 under the regulation of a CMV promoter. 1 µg of plasmid was transfected via lipofection using Lipofectamine 2000 reagent (ThermoFisher), in medium free of antibiotics and antifungals. Normal medium was replaced after 4 h. After 24 h of expression, cells were treated with 0.1, 0.3 or 1 mM H_2O_2 for 2 h, washed with PBS and fixed with 4 % PFA for 20 minutes.

For non-transfected cells, 50,000 cells were seeded and treated with H_2O_2 the next day as described above.

Cell survival assay

10,000 cells were seeded in wells of a 96-well plate in RPMI medium supplemented with 10% FBS. After two days cells were treated with H_2O_2 for 1 h. PrestoBlue reagent (Invitrogen) was added to a final concentration of 10% and was incubated for additional 1 h. PrestoBlue incubation time was taken into account for total treatment time. Fluorescence was measured at 590 nm with 560 nm excitation wavelength.

Immunocytochemistry

For fixed cells, membrane permeabilization was achieved with 0.5% Triton-X for 5 min. Samples were blocked with 2% BSA for 1 h at room temperature, and primary antibodies were applied overnight in blocking reagent at 4 °C. Anti-hSSB1 (HPA044615), anti-G3BP1 (ab56574), and anti-SK1-Hedls (sc-8418) were purchased from Sigma-Aldrich, Abcam, and Santa Cruz Biotechnology, respectively. Secondary antibodies (anti-mouse IgG AF647, anti-rabbit AF647, Thermo), conjugated with fluorophore (AF647) were used for fluorescence labeling. The coverslips, coated with immunostained cells were immobilized using Mowiol 4.88 (Polysciences) (supplemented with DAPI) on microscope slides.

Epifluorescence and confocal microscopy of immunostained cells

For epifluorescence microscopy of immunostained HeLa cells, a Zeiss Cell Observer Z1 microscope was used with a plan-apochromat 63x oil immersion objective with a numerical aperture of 1.46. 12-bit images were captured at a pixel size of 1388 x 1040. LED module light sources were used for excitation at 385 nm, 475 nm, and 630 nm with excitation/emission filter setups of 335-383/420-470, 450-490/500-550, 625-655/665-715 nm, respectively. An AxioCam MR R3 camera (Zeiss) was used for fluorescence detection.

For confocal microscopy, a Zeiss LSM 800 microscope was used with a plan-apochromat 63x oil immersion objective with a numerical aperture of 1.40. 16-bit images were obtained at 1437x1437 pixel size. For excitation, 405 nm, 488 nm, and 640 nm wavelength laser lights were used with pinhole sizes of 44 µm, 38 µm, and 44 µm, respectively. GaAsP photomultiplier tubes were used for fluorescence emission detection. Z-

stacks of 11 slices with an optical sectioning of 2.1 μm around the midplane of cells were imaged for colocalization analysis. For 3D reconstruction of cytoplasmic granules, Z-stacks of 16 slices with an optical sectioning of 3.6 μm were used. Imaging and 3D reconstruction were performed using ZENPro software.

Colocalization analysis

Colocalization analysis was performed on optically sectioned confocal images using ImageJ. First, maximal intensity projections were made on both green (hSSB1) and red (G3BP1) channels, separately. The newly generated maximal intensity projections were used for further analysis. Mean intensity of cytoplasmic G3BP1 droplets was measured and thresholds were set on both projected images as the minimum of the observed mean intensity of G3BP1 droplets. Since hSSB1 has a strong nuclear signal, nuclei were manually deleted from hSSB1 intensity projections before thresholding. The thresholded images were used for calculating Manders split and object-based colocalization coefficients. Manders coefficient is proportional to the amount of fluorescence of the colocalizing pixels in each color channel. Values range from 0 to 1, expressing the fraction of intensity in a channel that is located in pixels where there is above-threshold intensity in the other color channel. Data were obtained from 5 different images with ~100 G3BP1 droplets in each, together with standard deviation. Object-based colocalization analysis shows the ratios of centers of mass coincidence for particles detected in both channels using the thresholds described above. Data were obtained from 5 different images with ~100 G3BP1 droplets in each, together with standard deviation. The analysis described above was performed using the JaCoP plugin in ImageJ (*48*).

Determination of nuclear and cytoplasmic hSSB1 intensities

Using the epifluorescence microscopy setup described above, we obtained 4 x 4 tile images at each different condition in order to achieve a sufficient sample size of around 400 cells per image. The tiles were stitched together using ZENPro. Nuclei were detected as ROIs based on DAPI signal. Mean fluorescence intensities of hSSB1 signal were measured on nuclear ROIs. For two-sample T-tests, mean nuclear intensities were randomly divided into 5 groups and averaged. Thus, T-tests were performed on these n = 5 average intensities from each condition.

Cell typization

To determine whether hSSB1 overexpression influences the fraction of cells forming stress granules (SG+), we devised a method to quantify the number of SG+ cells upon H_2O_2 treatment when either EGFP or hSSB1-GFP is overexpressed. Using the epifluorescence microscopy setup described above, we obtained 4x4 tile images at each condition in order to achieve a sufficient sample size. Tiles were stitched together using ZENPro, and the full image was equally divided into 4 subimages, which were analyzed separately. Outlines of cells were detected based on G3BP1 signal using Cellpose deep learning-based algorithm (*49*). The detected outlines were imported to ImageJ as ROIs. Thus, each ROI represented a different cell in the image. Mean intensity, Skewness and Kurtosis (third and fourth order moment about the mean) were measured on ROIs. A cell was considered as EGFP+ if its mean fluorescence intensity in the green channel was higher than the mean intensity of the predetermined green autofluorescence of a HeLa cell in the applied imaging setup. Skewness and Kurtosis was indicative of the heterogenous distribution of the G3BP1 fluorescence signal in the cytoplasm. The more SGs were seen, the higher Skewness and Kurtosis values were obtained. Thus, a cell was considered SG+ if both Skewness and Kurtosis were higher than their predetermined thresholds of 1 and 5, respectively. Cell typization was done on all 4

subimages (n = 4) at the given condition. Means ± SEM (standard error of mean) values are reported.

Quantification and statistical analysis

Data analysis and visualization was performed using OriginLab 8.0 (Microcal corp.). Pixel densitometry was performed using GelQuant Pro software v12 (DNR Bio Imaging Ltd.). T-tests were performed in OriginLab 8.0. Significance levels are indicated in the figure legends.

REFERENCES

1. R. D. Shereda, A. G. Kozlov, T. M. Lohman, M. M. Cox, J. L. Keck, SSB as an organizer/mobilizer of genome maintenance complexes. *Crit Rev Biochem Mol Biol*. **43**, 289–318 (2008).
2. E. Antony, T. M. Lohman, Dynamics of E. coli single stranded DNA binding (SSB) protein-DNA complexes. *Semin Cell Dev Biol*. **86**, 102–111 (2019).
3. N. W. Ashton, D. Loo, N. Paquet, K. J. O'Byrne, D. J. Richard, Novel insight into the composition of human single-stranded DNA-binding protein 1 (hSSB1)-containing protein complexes. *BMC Mol Biol*. **17**, 24 (2016).
4. P. R. Bianco, S. Pottinger, H. Y. Tan, T. Nguyenduc, K. Rex, U. Varshney, The IDL of E. coli SSB links ssDNA and protein binding by mediating protein-protein interactions. *Protein Sci*. **26**, 227–241 (2017).
5. D. J. Richard, E. Bolderson, L. Cubeddu, R. I. M. Wadsworth, K. Savage, G. G. Sharma, M. L. Nicolette, S. Tsvetanov, M. J. McIlwraith, R. K. Pandita, S. Takeda, R. T. Hay, J. Gautier, S. C. West, T. T. Paull, T. K. Pandita, M. F. White, K. K. Khanna, Single-stranded DNA-binding protein hSSB1 is critical for genomic stability. *Nature*. **453**, 677–81 (2008).
6. V. Vidhyasagar, Y. He, M. Guo, H. Ding, T. Talwar, V. Nguyen, J. Nwosu, G. Katselis, Y. Wu, C-termini are essential and distinct for nucleic acid binding of human NABP1 and NABP2. *Biochim Biophys Acta*. **1860**, 371–83 (2016).
7. T. Lawson, S. El-Kamand, R. Kariawasam, D. J. Richard, L. Cubeddu, R. Gamsjaeger, A Structural Perspective on the Regulation of Human Single-Stranded DNA Binding Protein 1 (hSSB1, OBFC2B) Function in DNA Repair. *Comput Struct Biotechnol J*. **17**, 441–446 (2019).
8. N. Paquet, M. N. Adams, V. Leong, N. W. Ashton, C. Touma, R. Gamsjaeger, L. Cubeddu, S. Beard, J. T. Burgess, E. Bolderson, K. J. O'Byrne, D. J. Richard, hSSB1 (NABP2/ OBFC2B) is required for the repair of 8-oxo-guanine by the hOGG1-mediated base excision repair pathway. *Nucleic Acids Res*. **43**, 8817–29 (2015).
9. R. K. Pandita, T. T. Chow, D. Udayakumar, A. L. Bain, L. Cubeddu, C. R. Hunt, W. Shi, N. Horikoshi, Y. Zhao, W. E. Wright, K. K. Khanna, J. W. Shay, T. K. Pandita, Single-Strand DNA-Binding Protein SSB1 Facilitates TERT Recruitment to Telomeres and Maintains Telomere G-Overhangs. *Cancer Res*. **75**, 858–869 (2015).
10. J. R. Skaar, A. L. Ferris, X. Wu, A. Saraf, K. K. Khanna, L. Florens, M. P. Washburn, S. H. Hughes, M. Pagano, The Integrator complex controls the termination of transcription at diverse classes of gene targets. *Cell Res*. **25**, 288–305 (2015).
11. N. Feldhahn, E. Ferretti, D. F. Robbiani, E. Callen, S. Deroubaix, L. Selleri, A. Nussenzweig, M. C. Nussenzweig, The hSSB1 orthologue Obfc2b is essential for skeletogenesis but dispensable for the DNA damage response in vivo. *EMBO J*. **31**, 4045–56 (2012).

12. L. V Croft, E. Bolderson, M. N. Adams, S. El-Kamand, R. Kariawasam, L. Cubeddu, R. Gamsjaeger, D. J. Richard, Human single-stranded DNA binding protein 1 (hSSB1, OBFC2B), a critical component of the DNA damage response. *Semin Cell Dev Biol*. **86**, 121–128 (2019).
13. D. J. Richard, L. Cubeddu, A. J. Urquhart, A. Bain, E. Bolderson, D. Menon, M. F. White, K. K. Khanna, hSSB1 interacts directly with the MRN complex stimulating its recruitment to DNA double-strand breaks and its endo-nuclease activity. *Nucleic Acids Res*. **39**, 3643–51 (2011).
14. S.-H. Yang, R. Zhou, J. Campbell, J. Chen, T. Ha, T. T. Paull, The SOSS1 single-stranded DNA binding complex promotes DNA end resection in concert with Exo1. *EMBO J*. **32**, 126–39 (2013).
15. L. V Croft, N. W. Ashton, N. Paquet, E. Bolderson, K. J. O'Byrne, D. J. Richard, hSSB1 associates with and promotes stability of the BLM helicase. *BMC Mol Biol*. **18**, 13 (2017).
16. E. Bolderson, E. Petermann, L. Croft, A. Suraweera, R. K. Pandita, T. K. Pandita, T. Helleday, K. K. Khanna, D. J. Richard, Human single-stranded DNA binding protein 1 (hSSB1/NABP2) is required for the stability and repair of stalled replication forks. *Nucleic Acids Res*. **42**, 6326–36 (2014).
17. N. Paquet, M. N. Adams, N. W. Ashton, C. Touma, R. Gamsjaeger, L. Cubeddu, V. Leong, S. Beard, E. Bolderson, C. H. Botting, K. J. O'Byrne, D. J. Richard, hSSB1 (NABP2/OBFC2B) is regulated by oxidative stress. *Sci Rep*. **6**, 27446 (2016).
18. C. Touma, M. N. Adams, N. W. Ashton, M. Mizzi, S. El-Kamand, D. J. Richard, L. Cubeddu, R. Gamsjaeger, A data-driven structural model of hSSB1 (NABP2/OBFC2B) self-oligomerization. *Nucleic Acids Res*. **45**, 8609–8620 (2017).
19. W. Ren, H. Chen, Q. Sun, X. Tang, S. C. Lim, J. Huang, H. Song, Structural basis of SOSS1 complex assembly and recognition of ssDNA. *Cell Rep*. **6**, 982–991 (2014).
20. J. Huang, Z. Gong, G. Ghosal, J. Chen, SOSS complexes participate in the maintenance of genomic stability. *Mol Cell*. **35**, 384–93 (2009).
21. J. R. Skaar, D. J. Richard, A. Saraf, A. Toschi, E. Bolderson, L. Florens, M. P. Washburn, K. K. Khanna, M. Pagano, INTS3 controls the hSSB1-mediated DNA damage response. *J Cell Biol*. **187**, 25–32 (2009).
22. Y. Li, E. Bolderson, R. Kumar, P. A. Muniandy, Y. Xue, D. J. Richard, M. Seidman, T. K. Pandita, K. K. Khanna, W. Wang, HSSB1 and hSSB2 form similar multiprotein complexes that participate in DNA damage response. *J Biol Chem*. **284**, 23525–31 (2009).
23. G. M. Harami, Z. J. Kovács, R. Pancsa, J. Pálinkás, V. Baráth, K. Tárnok, A. Málnási-Csizmadia, M. Kovács, Phase separation by ssDNA binding protein controlled via protein−protein and protein−DNA interactions. *Proceedings of the National Academy of Sciences*. **117**, 26206–26217 (2020).
24. T. Zhao, Y. Liu, Z. Wang, R. He, J. Xiang Zhang, F. Xu, M. Lei, M. B. Deci, J. Nguyen, P. R. Bianco, Super-resolution imaging reveals changes in Escherichia coli SSB localization in response to DNA damage. *Genes Cells*. **24**, 814–826 (2019).
25. H. Sies, D. P. Jones, Reactive oxygen species (ROS) as pleiotropic physiological signalling agents. *Nat Rev Mol Cell Biol*. **21**, 363–383 (2020).
26. A. G. Kozlov, X. Cheng, H. Zhang, M. K. Shinn, E. Weiland, B. Nguyen, I. A. Shkel, E. Zytkiewicz, I. J. Finkelstein, M. T. Record, T. M. Lohman, How Glutamate Promotes Liquid-liquid Phase Separation and DNA Binding Cooperativity of E. coli SSB Protein. *J Mol Biol*. **434**, 167562 (2022).
27. G. L. Dignon, R. B. Best, J. Mittal, Biomolecular Phase Separation: From Molecular Driving Forces to Macroscopic Properties. *Annu Rev Phys Chem*. **71**, 53–75 (2020).

28. S. F. Banani, H. O. Lee, A. A. Hyman, M. K. Rosen, Biomolecular condensates: organizers of cellular biochemistry. *Nat Rev Mol Cell Biol*. **18**, 285–298 (2017).
29. J. R. Buchan, R. Parker, Eukaryotic stress granules: the ins and outs of translation. *Mol Cell*. **36**, 932–41 (2009).
30. D. S. W. Protter, R. Parker, Principles and Properties of Stress Granules. *Trends Cell Biol*. **26**, 668–679 (2016).
31. P. Yang, C. Mathieu, R.-M. Kolaitis, P. Zhang, J. Messing, U. Yurtsever, Z. Yang, J. Wu, Y. Li, Q. Pan, J. Yu, E. W. Martin, T. Mittag, H. J. Kim, J. P. Taylor, G3BP1 Is a Tunable Switch that Triggers Phase Separation to Assemble Stress Granules. *Cell*. **181**, 325-345.e28 (2020).
32. D. Ganini, F. Leinisch, A. Kumar, J. Jiang, E. J. Tokar, C. C. Malone, R. M. Petrovich, R. P. Mason, Fluorescent proteins such as eGFP lead to catalytic oxidative stress in cells. *Redox Biol*. **12**, 462–468 (2017).
33. J.-Y. Youn, B. J. A. Dyakov, J. Zhang, J. D. R. Knight, R. M. Vernon, J. D. Forman-Kay, A.-C. Gingras, Properties of Stress Granule and P-Body Proteomes. *Mol Cell*. **76**, 286–294 (2019).
34. Y. Luo, Z. Na, S. A. Slavoff, P-Bodies: Composition, Properties, and Functions. *Biochemistry*. **57**, 2424–2431 (2018).
35. M. E. Johnson, A. V Grassetti, J. N. Taroni, S. M. Lyons, D. Schweppe, J. K. Gordon, R. F. Spiera, R. Lafyatis, P. J. Anderson, S. A. Gerber, M. L. Whitfield, Stress granules and RNA processing bodies are novel autoantibody targets in systemic sclerosis. *Arthritis Res Ther*. **18**, 27 (2016).
36. M. Schieber, N. S. Chandel, ROS function in redox signaling and oxidative stress. *Curr Biol*. **24**, R453-62 (2014).
37. S. Maynard, S. H. Schurman, C. Harboe, N. C. de Souza-Pinto, V. A. Bohr, Base excision repair of oxidative DNA damage and association with cancer and aging. *Carcinogenesis*. **30**, 2–10 (2009).
38. C. E. Paulsen, K. S. Carroll, Orchestrating redox signaling networks through regulatory cysteine switches. *ACS Chem Biol*. **5**, 47–62 (2010).
39. L. B. Poole, The basics of thiols and cysteines in redox biology and chemistry. *Free Radic Biol Med*. **80**, 148–57 (2015).
40. S. El-Kamand, S. Jergic, T. Lawson, R. Kariawasam, D. J. Richard, L. Cubeddu, R. Gamsjaeger, *bioRxiv*, in press, doi:10.1101/2020.08.26.269084.
41. C. Klomsiri, P. A. Karplus, L. B. Poole, Cysteine-based redox switches in enzymes. *Antioxid Redox Signal*. **14**, 1065–77 (2011).
42. X. Huang, S. Chen, W. Li, L. Tang, Y. Zhang, N. Yang, Y. Zou, X. Zhai, N. Xiao, W. Liu, P. Li, C. Xu, ROS regulated reversible protein phase separation synchronizes plant flowering. *Nat Chem Biol*. **17**, 549–557 (2021).
43. M. Kato, Y.-S. Yang, B. M. Sutter, Y. Wang, S. L. McKnight, B. P. Tu, Redox State Controls Phase Separation of the Yeast Ataxin-2 Protein via Reversible Oxidation of Its Methionine-Rich Low-Complexity Domain. *Cell*. **177**, 711-721.e8 (2019).
44. H. Marmor-Kollet, A. Siany, N. Kedersha, N. Knafo, N. Rivkin, Y. M. Danino, T. G. Moens, T. Olender, D. Sheban, N. Cohen, T. Dadosh, Y. Addadi, R. Ravid, C. Eitan, B. Toth Cohen, S. Hofmann, C. L. Riggs, V. M. Advani, A. Higginbottom, J. Cooper-Knock, J. H. Hanna, Y. Merbl, L. Van Den Bosch, P. Anderson, P. Ivanov, T. Geiger, E. Hornstein, Spatiotemporal Proteomic Analysis of Stress Granule Disassembly Using APEX Reveals Regulation by SUMOylation and Links to ALS Pathogenesis. *Mol Cell*. **80**, 876-891.e6 (2020).
45. M. N. Adams, L. V Croft, A. Urquhart, M. A. M. Saleem, A. Rockstroh, P. H. G. Duijf, P. B. Thomas, G. P. Ferguson, I. M. Najib, E. T. Shah, E. Bolderson, S. Nagaraj, E. D.

Williams, C. C. Nelson, K. J. O'Byrne, D. J. Richard, hSSB1 (NABP2/OBFC2B) modulates the DNA damage and androgen-induced transcriptional response in prostate cancer. *Prostate*. **83**, 628–640 (2023).
46. V. Vidhyasagar, Y. He, M. Guo, T. Talwar, R. S. Singh, M. Yadav, G. Katselis, F. J. Vizeacoumar, K. E. Lukong, Y. Wu, Biochemical characterization of INTS3 and C9ORF80, two subunits of hNABP1/2 heterotrimeric complex in nucleic acid binding. *Biochem J*. **475**, 45–60 (2018).
47. G. M. Harami, J. Pálinkás, Y. Seol, Z. J. Kovács, M. Gyimesi, H. Harami-Papp, K. C. Neuman, M. Kovács, The toposiomerase IIIalpha-RMI1-RMI2 complex orients human Bloom's syndrome helicase for efficient disruption of D-loops. *Nat Commun*. **13**, 654 (2022).
48. S. Bolte, F. P. Cordelières, A guided tour into subcellular colocalization analysis in light microscopy. *J Microsc*. **224**, 213–32 (2006).
49. C. Stringer, T. Wang, M. Michaelos, M. Pachitariu, Cellpose: a generalist algorithm for cellular segmentation. *Nat Methods*. **18**, 100–106 (2021).

ACKNOWLEDGMENTS

Funding: This work was supported by the "Momentum" Program of the Hungarian Academy of Sciences (LP2011-006/2011), ELTE KMOP-4.2.1/B-10-2011-0002, NKFIH K-123989, and NKFIH K-134595 grants to M.K. The project was supported by the NRDIO (VEKOP-2.3.3-15-2016-00007 to ELTE) grant. G.M.H. was supported by the Premium Postdoctoral Program of the Hungarian Academy of Sciences (PREMIUM-2017-17 to G.M.H.). Z.J.K. and J.P. were supported by the New National Excellence Program of the Ministry for Innovation and Technology (Grants ÚNKP-21-3 to Z.J.K. and ÚNKP-19-2 to J.P.), and the Co-operative Doctoral Program of the Ministry of Innovation and Technology financed from the National Research, Development and Innovation Fund. This work was completed in the ELTE "SzintPlusz" Thematic Excellence Programme supported by the Hungarian Ministry for Innovation and Technology, and also in the framework of Project no. 2018-1.2.1-NKP-2018-00005 implemented with the support provided from the National Research, Development and Innovation Fund of Hungary, financed under the 2018-1.2.1-NKP funding scheme.

Author contributions: GMH, JP, ZJK, GS, and MK conceptualized the project and designed experiments. GMH, JP, ZJK, KT, HHP, JH, LM, NK, and ST performed experiments and analyzed the data. GMH, JP, ZJK, and KM wrote the paper. All authors participated in revising the manuscript.

Competing interests: The authors declare no competing interests.

Data and materials availability: PDB files 4MZ9, 5D8E, 5D8F and 4OWW were obtained from the Protein Data Bank. hSSB1 expression levels were obtained from Expression Atlas (https://www.ebi.ac.uk/gxa/home). All data needed to evaluate the conclusions in the paper are present in the paper and/or the Supplementary Materials.

FIGURES AND TABLES

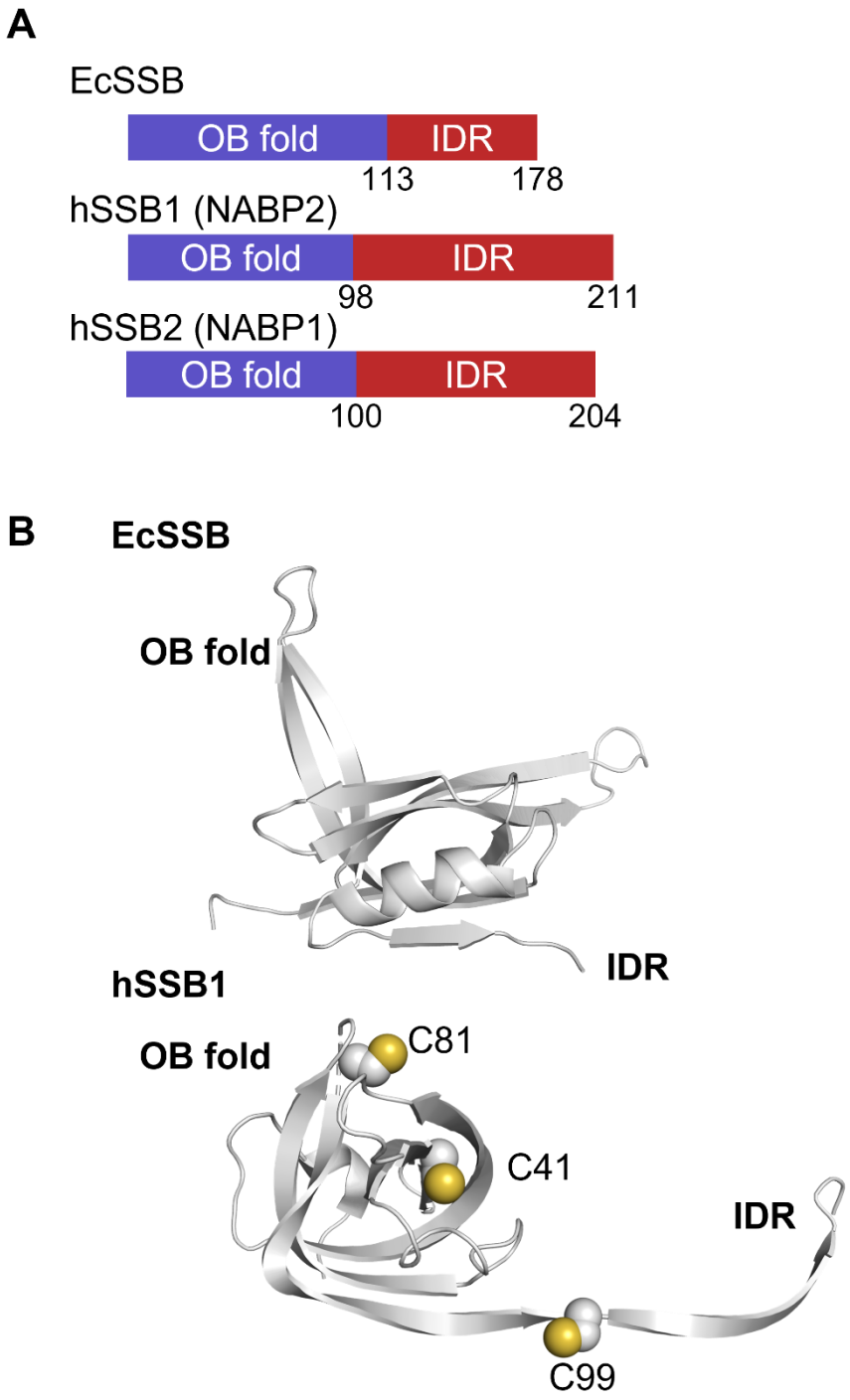

Fig. 1. Bacterial and human SSB proteins show high structural similarity. (A) Domain structure of *E. coli* (Ec) and human (h) SSB proteins, with amino acid positions indicated at domain boundaries. **(B)** Three-dimensional structures of EcSSB (PDB code 4MZ9) and hSSB1 (5D8F), with cysteine residues highlighted. (EcSSB contains no cysteines.) Structures shown are visible until aa 114 and 110, respectively.

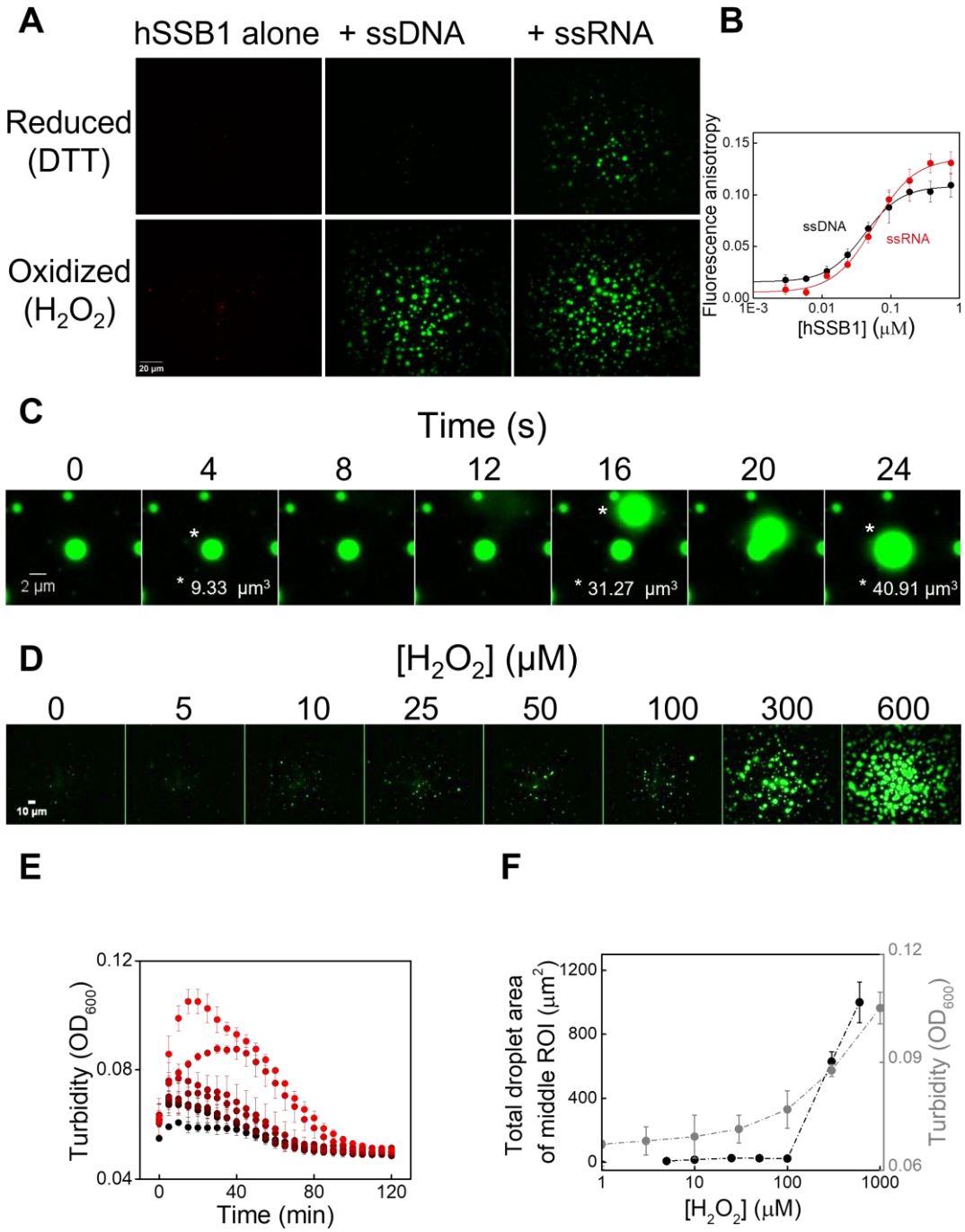

Fig. 2. hSSB1 forms ssDNA and ssRNA nucleoprotein coacervates in a redox-dependent manner. (A) ssDNA and ssRNA induce hSSB1 LLPS in oxidative conditions. Representative epifluorescence microscopy images (*n* = 3 independent measurements) of hSSB1 (5 µM monomer concentration) were obtained in the absence of nucleic acids using AlexaFluor647-labeled hSSB1 (0.1 µM), and in the presence of ssDNA (2 µM dT_{45} containing 0.1 µM Cy3-dT_{45}) and ssRNA (2 µM U_{41} containing 41-mer Cy3-labeled nonhomopolymeric ssRNA) (cf. **fig. S2**) in reducing (1 mM DTT) and oxidizing (980 µM H_2O_2) conditions. **(B)** ssDNA and ssRNA (10 nM 3'-fluorescein labeled nonhomopolymeric 36-mer) binding by hSSB1 measured with fluorescence anisotropy titrations. Solid lines show fits using the Hill equation. Means ± SEM are shown for *n* = 3 independent experiments. Determined equilibrium

dissociation constants (K_d) and Hill-coefficients (n) are shown in **Table S1**. **(C)** Droplet fusion, volume additivity, and spherical morphology support liquid-like behavior of hSSB1 droplets. Time-lapse fluorescence images of fusion of hSSB1 droplets (5 μM) are shown, recorded in the presence of labeled ssDNA (2 μM dT_{79} containing 0.1 μM Cy3-dT_{79}) and H_2O_2 (980 μM). **(D)** H_2O_2 concentration dependence of the appearance of hSSB1 droplets (5 μM hSSB1, 2 μM dT_{79} containing 0.1 μM Cy3-dT_{79}). **(E)** Time-dependent turbidity measurements showing hSSB1 LLPS even at low micromolar H_2O_2 concentrations (2 μM hSSB1, 1 μM dT_{79} ssDNA; H_2O_2 concentrations from bottom to top were 0, 1, 3, 10, 30, 100, 300, and 1000 μM). Error bars represent SEM for n = 3 independent experiments. (**F**) H_2O_2 concentration dependence of total droplet area of middle ROIs in microscopy images (panel **D**) and maximal OD values from panel **E**. Error bars represent SEM for n = 3 independent measurements.

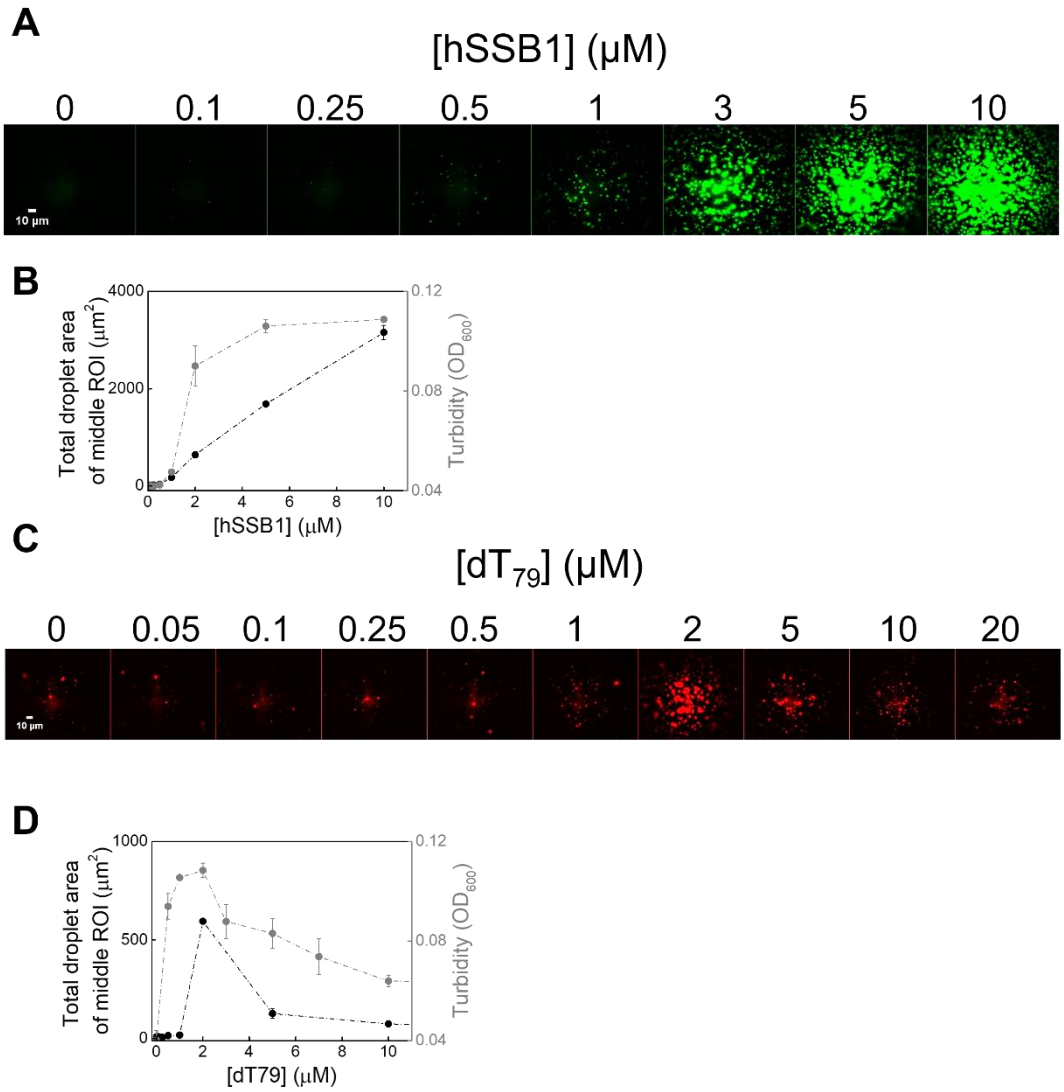

Fig. 3. hSSB1 nucleoprotein condensation occurs in a stoichiometric fashion, with a bell-shaped dependence on nucleic acid concentration. (A) Epifluorescence microscopy images (*n* = 3 independent measurements) recorded in the presence of labeled ssDNA (2 μM dT_{79} containing 0.1 μM Cy3-dT_{79}) and H_2O_2 (980 μM) showing that hSSB1 droplets become apparent at 1 μM protein concentration. **(B)** hSSB1 concentration dependence of total droplet area of middle ROIs in microscopic images (panel **A**) and OD_{600} values from turbidity measurements in the presence of ssDNA (2 μM dT_{79}) and H_2O_2 (980 μM). Error bars represent SEM for *n* = 3 independent measurements. **(C)** Epifluorescence microscopic images (*n* = 3 independent measurements) of fluorescently labeled hSSB1 droplets (5 μM hSSB1 containing 0.1 μM Alexa Fluor647-labeled hSSB1) titrated with dT_{79} in the presence of 980 μM H_2O_2. **(D)** dT_{79} concentration dependence of total droplet areas from fluorescence microscopy experiments shown in panel **C** and OD_{600} values from turbidity measurements using 5 μM hSSB1 in the presence of 980 μM H_2O_2. Error bars represent SEM for *n* = 3 independent measurements.

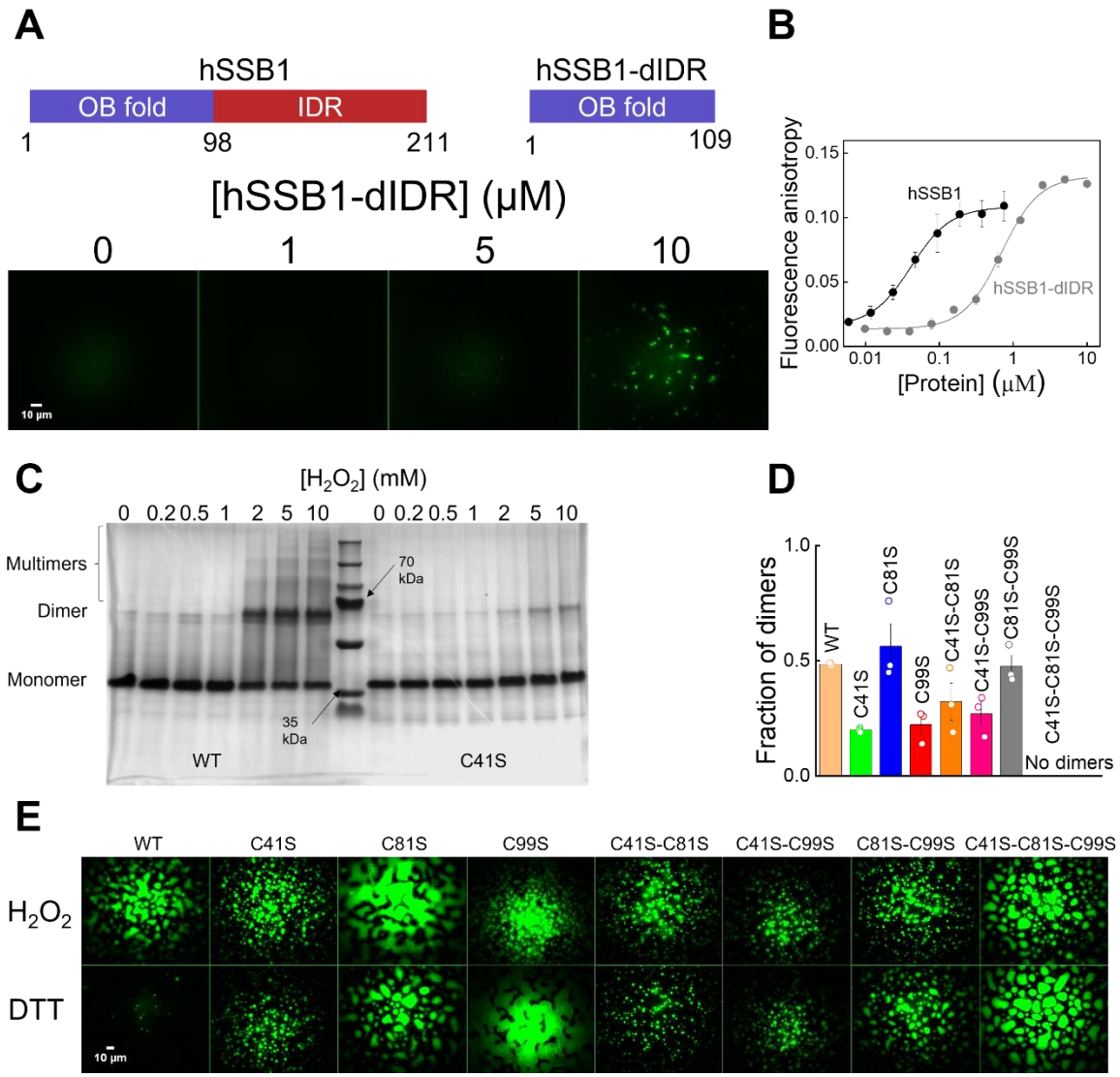

Fig. 4. Intrinsically disordered region (IDR) of hSSB1 is indispensable for LLPS propensity, cysteines 41 and 99 mediate covalent oligomerization, while all hSSB1 cysteines are required for redox-sensitive condensation. (A) Domain structure of hSSB1 WT and hSSB1-dIDR constructs (top panel). Epifluorescence images (n = 3 independent measurements) of hSSB1-dIDR in the presence of labeled ssDNA (2 μM dT_{79} containing 0.1 μM Cy3-dT_{79}) and H_2O_2 (980 μM) show no droplet formation, only amorphous aggregates at high protein concentration (bottom panel). **(B)** ssDNA (10 nM 3'-fluorescein labeled nonhomopolymeric 36-mer) binding of hSSB1 and hSSB1-IDR measured in fluorescence anisotropy titrations show a marked decrease in the ssDNA affinity of hSSB1-dIDR compared to hSSB1 WT. Solid lines show fits using the Hill equation. Means ± SEM are shown for n = 3 independent measurements. Determined equilibrium dissociation constants (K_d) and Hill coefficients (n) are shown in **Table S1**. **(C)** A representative electrophoretogram (n = 3 independent measurements) of WT and C41S hSSB1 variants shows changes in monomer : dimer ratio in response to H_2O_2 treatment. Densitometric analysis was applied to determine relative protein amounts in individual fractions (cf. **fig. S7**). Monomers and dimers separated clearly in every case, while higher-order structures were distinguishable only in some cases, and thus omitted from the analysis. Note that the electrophoretic mobility of monomeric

hSSB1 is lower than expected based on its molecular weight of 22 kDa, which is a frequently observed feature for proteins containing long ID regions. Please note that each oxidation reaction contained < 100 µM DTT reducing agent originating from the storage buffer of hSSB1 constructs. **(D)** Fraction of dimers formed by hSSB1 variants in response to the highest applied H_2O_2 concentration (10 mM) (cf. **fig. S7**). The data indicate the key contributions of C41 and C99 to covalent dimerization (see Results). Means ± SEM are shown together with individual data points from n = 3 independent measurements. **(E)** Epifluorescence microscopy images (n = 3 independent measurements) showing that all hSSB1 variants retained their ability to undergo LLPS, but the redox sensitivity was lost for all non-WT cysteine variants (5 µM protein, 2 µM dT_{79} containing 0.1 µM dT_{79} ssDNA, 980 µM H_2O_2 or 1 mM DTT were present in all samples).

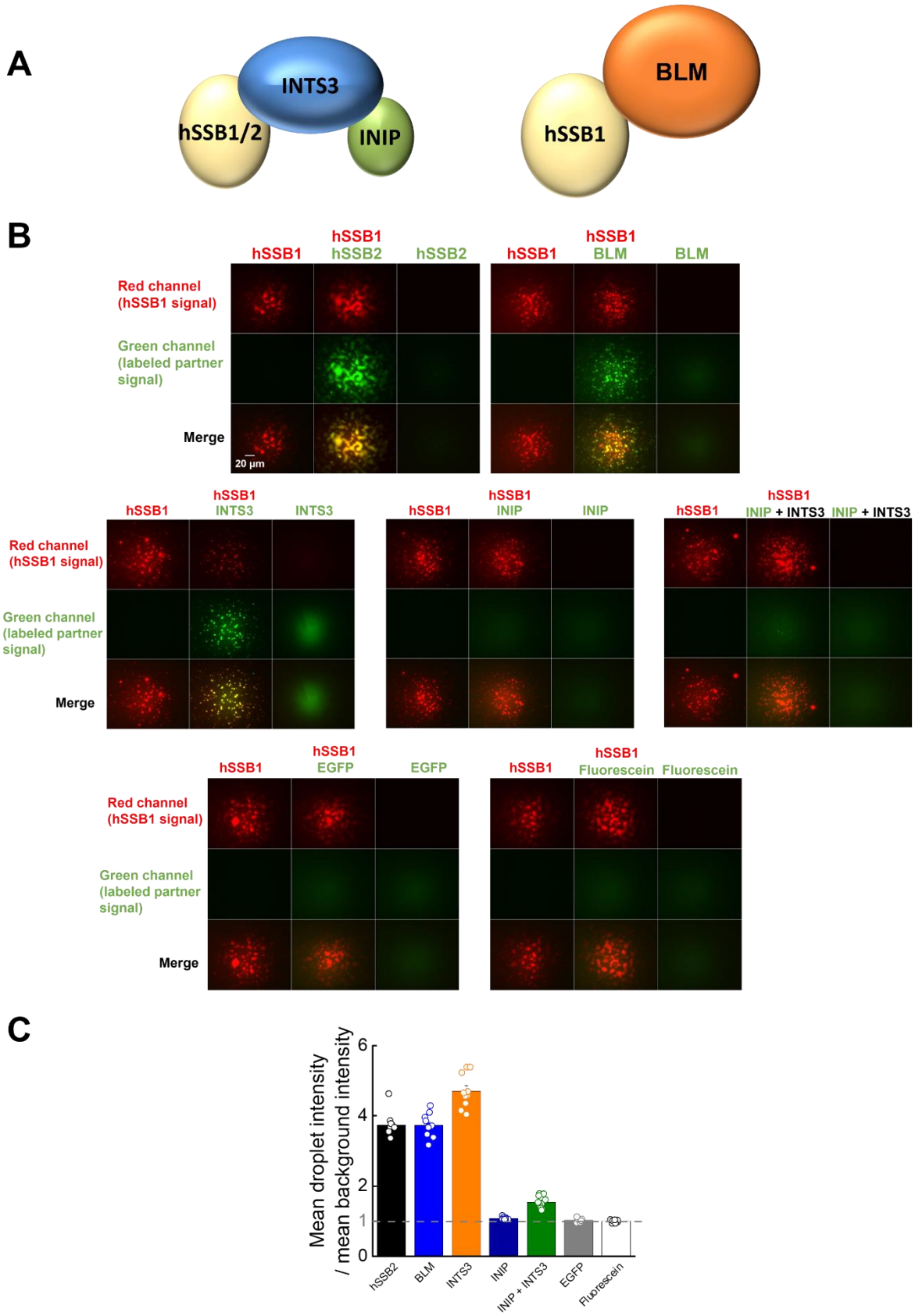

Fig. 5. Genome maintenance proteins are selectively enriched inside hSSB1 droplets, reflecting interaction-based control of their content. (A) Schematic illustration of SOSS and hSSB1-BLM helicase complexes. INTS3 interacts both with INIP and hSSB1, while there is no direct interaction between INIP and hSSB1. hSSB2 can replace hSSB1 in the SOSS

complex. **(B)** Two-channel fluorescence microscopy images (*n = 3* independent measurements) showing enrichment of proteins inside hSSB1 droplets. Columns represent three separate experiments (hSSB1, hSSB1 + partner, partner alone), while rows represent fluorescence channels. 5 µM hSSB1 with 0.1 µM AlexaFluor647-labeled hSSB1 were present in the samples, together with ssDNA (2 µM dT_{79}) and H_2O_2 (980 µM). 180 nM labeled interaction partner was used. In experiments containing labeled INTS3, labeled ssDNA (2 µM dT_{79} containing 0.1 µM Cy3-dT_{79}) was used to visualize hSSB1 droplets (5 µM unlabeled protein). See Materials and Methods for further details. Red channel shows hSSB1 droplets, green channel shows labeled interaction partners. Yellow color indicates co-condensation. Images were not background corrected. **(C)** Enrichment of various components in hSSB1 droplets, calculated as the ratio of the mean signal intensity within droplets and the mean background intensity, determined from background-uncorrected fluorescence images recorded for the indicated fluorescent molecules shown in panel **B**. A molecule is enriched inside hSSB1 droplets if the mentioned signal ratio is significantly higher than unity. Means ± SEM are shown together with individual data points of 10 images from *n* = 3 independent measurements.

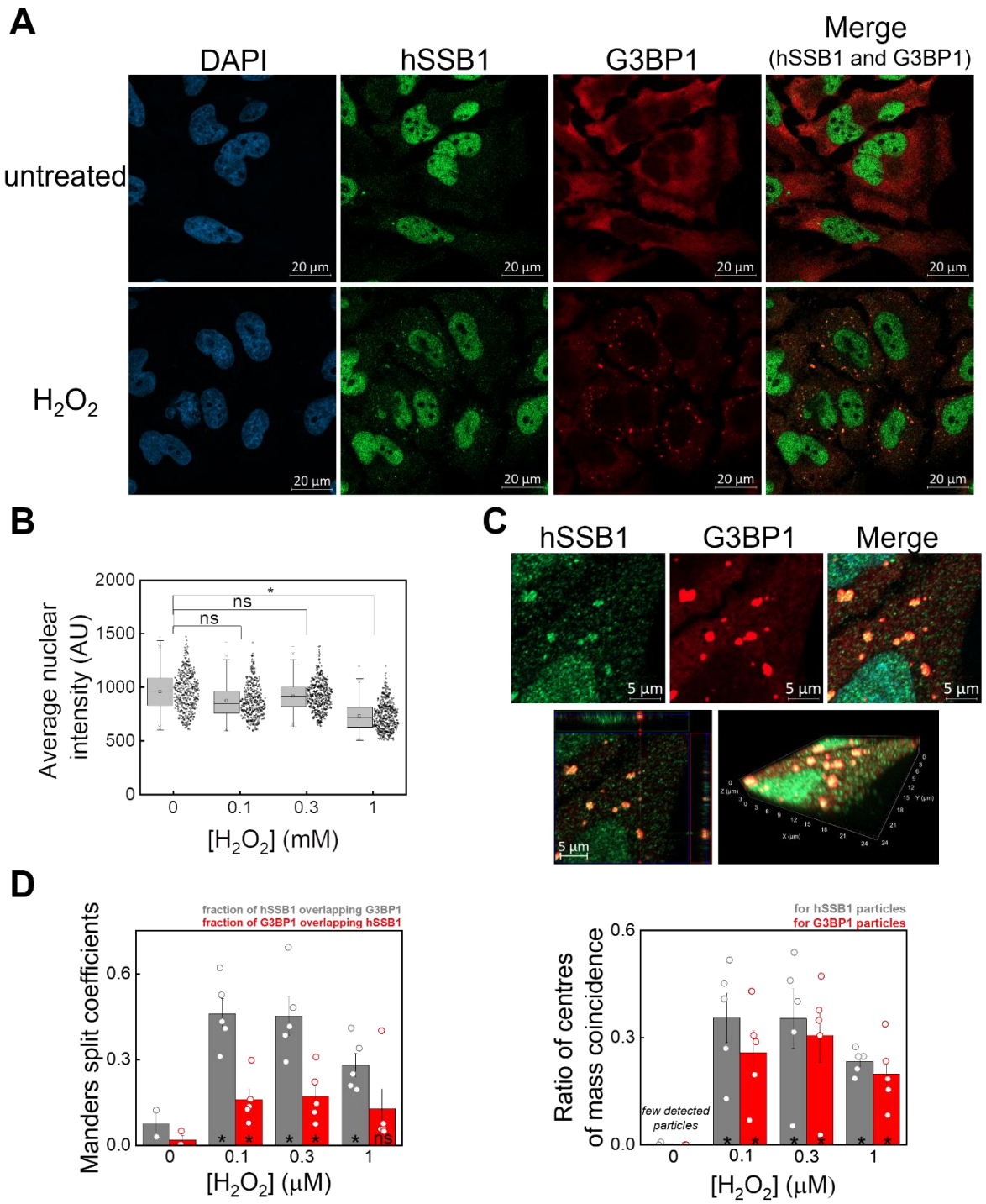

Fig. 6. hSSB1 is organized into cytoplasmic foci upon oxidative stress, colocalizing with stress granules. (A) Representative confocal microscopy images (n = 3 independent experiments) of immunostained, untreated or H_2O_2-treated (300 µM, 2 h) HeLa cells. Blue channel shows nuclear DAPI stain, green and red channels show endogenous hSSB1 and G3BP1 stress granule marker, respectively. Merge image was created from hSSB1 and G3BP1 channels; yellow color indicates colocalization. **(B)** Average nuclear hSSB1 intensity of immunostained HeLa cells decreases upon 1 mM H_2O_2 treatment (two-sample T-test, * indicates $p < 0.05$, see Materials and Methods; AU, arbitrary units). **(C)** Top row, magnified confocal images of a H_2O_2-treated HeLa cell (cf. panel **A**), with hSSB1 and G3BP1 showing colocalized enrichment in cytoplasmic granules. Bottom row, 3D reconstructed images of the

same ROI from confocal Z-stack images. Green and red channels show endogenous hSSB1 and G3BP1 stress granule marker, respectively; yellow color indicates colocalization. **(D)** Manders split coefficients (left) and object based colocalization (right) of hSSB1 and G3BP1 signals. For H_2O_2-treated cells, * indicates statistically significant differences compared to untreated cells (two-sample T-test, $p < 0.05$). Ns, not significant. Means ± SEM are shown together with individual data points from $n = 5$ images, each containing ~ 100 G3BP1 granules (see Materials and Methods).

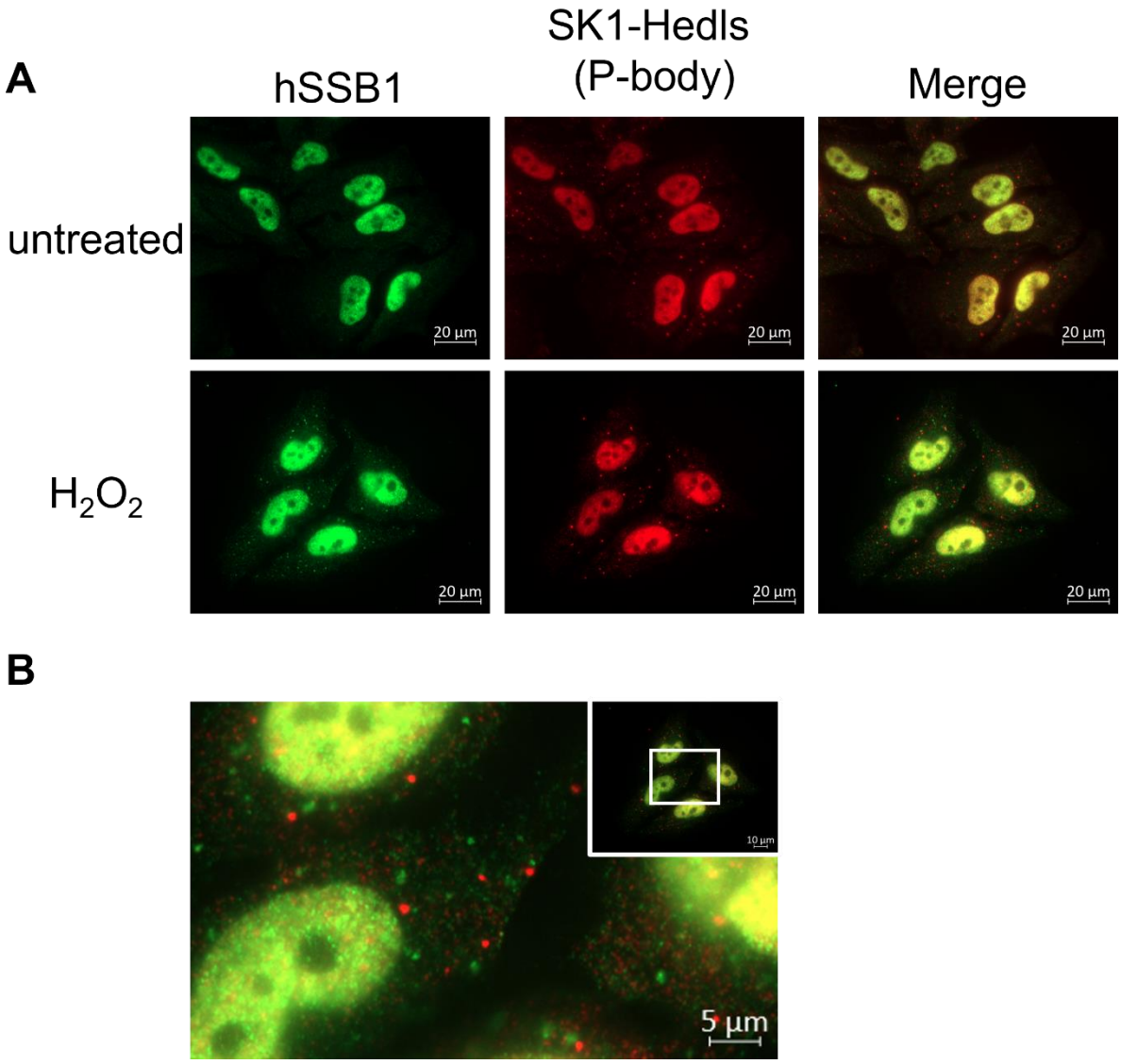

Fig. 7. Cytoplasmic hSSB1 granules do not colocalize with P-bodies. (A) Representative epifluorescence images (*n* = 3 independent measurements) of untreated and H_2O_2-treated (300 µM, 2 h) HeLa cells. Green and red channels show endogenous hSSB1 and SK1-Hedls P-body marker, respectively. Yellow color indicates colocalization. P-bodies were visible even in untreated cells, while hSSB1 granules formed only under oxidative stress conditions. (**B**) Magnified epifluorescence image of a H_2O_2-treated HeLa cell from panel **A**. No colocalization was observed between hSSB1 granules and P-bodies.

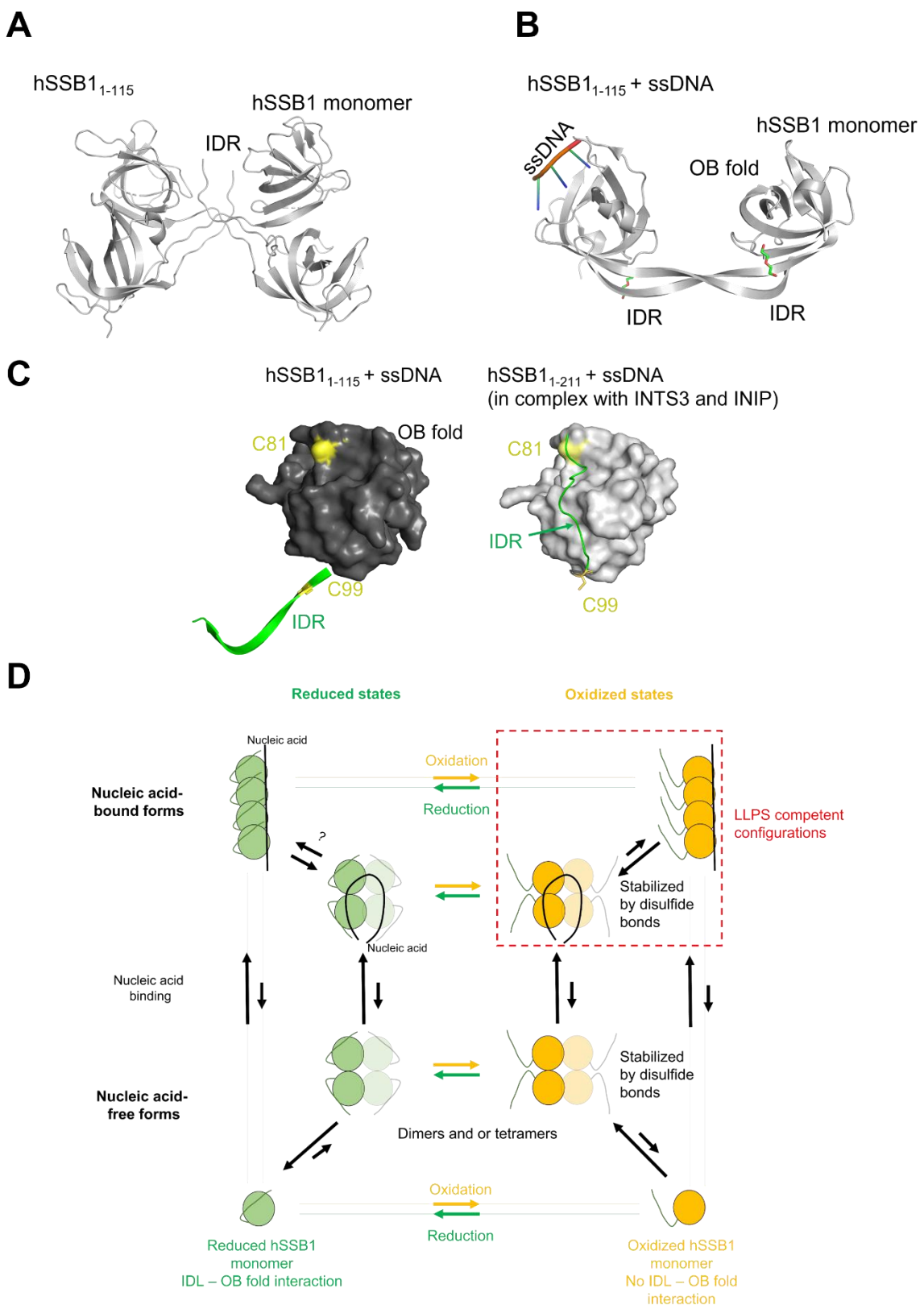

Fig. 8. Proposed model for the role of hSSB1 IDR tail flexibility in redox-dependent LLPS regulation. (A-B) Crystal structures of a truncated hSSB1 construct (amino acids 1-115) lacking the majority of the IDR, in the absence **(A)** and presence of ssDNA **(B)** (PDB codes 5D8E and 5D8F, respectively). In both conditions, interactions can be observed between the N-terminal IDR segment contained in the constructs. **(C)** Comparison of the

structure of ssDNA-bound truncated hSSB1 (dark grey, PDB code 5D8E, cf. panel **B**) and that of full-length hSSB1 in the ssDNA-bound SOSS1 complex (light grey, PDB code 4OWW; INTS3 and INIP structures were removed for clarity) (*19*). The N-terminal part of the IDR is not resolved in the latter structure. For both structures, the OB domain is shown as a surface model and the IDR tails are represented as green cartoons. Note the large difference between IDR conformations. **(D)** Proposed model for regulation of hSSB1 LLPS. In the reduced form and in the absence of nucleic acids, hSSB1 is in a dynamic equilibrium between monomeric and oligomeric states, with the monomeric form being favored (*6*, *17*). Binding to single-stranded nucleic acids may either stabilize/facilitate protein oligomerization, or hSSB1 monomers can bind independently to the nucleic acid lattice in a sequential order without formation of oligomers. Under reducing conditions, the C-terminal part of the hSSB1 IDR can interact with the OB fold (cf. panel **C**, right side) both in the absence and presence of nucleic acids. Upon oxidation, the IDR is released from the OB fold and participates in intermolecular IDR-IDR interactions (cf. panel **C**, left side). Covalent hSSB1 oligomers form via disulfide bridges involving C41 and C99; however, covalent oligomerization is not required for LLPS *per se* (cf. **Fig. 4D-E**). LLPS is triggered by multivalency brought about by nucleic acid binding (independent of hSSB1 oligomerization state) and oxidation-dependent, conformationally regulated IDR-IDR interactions.

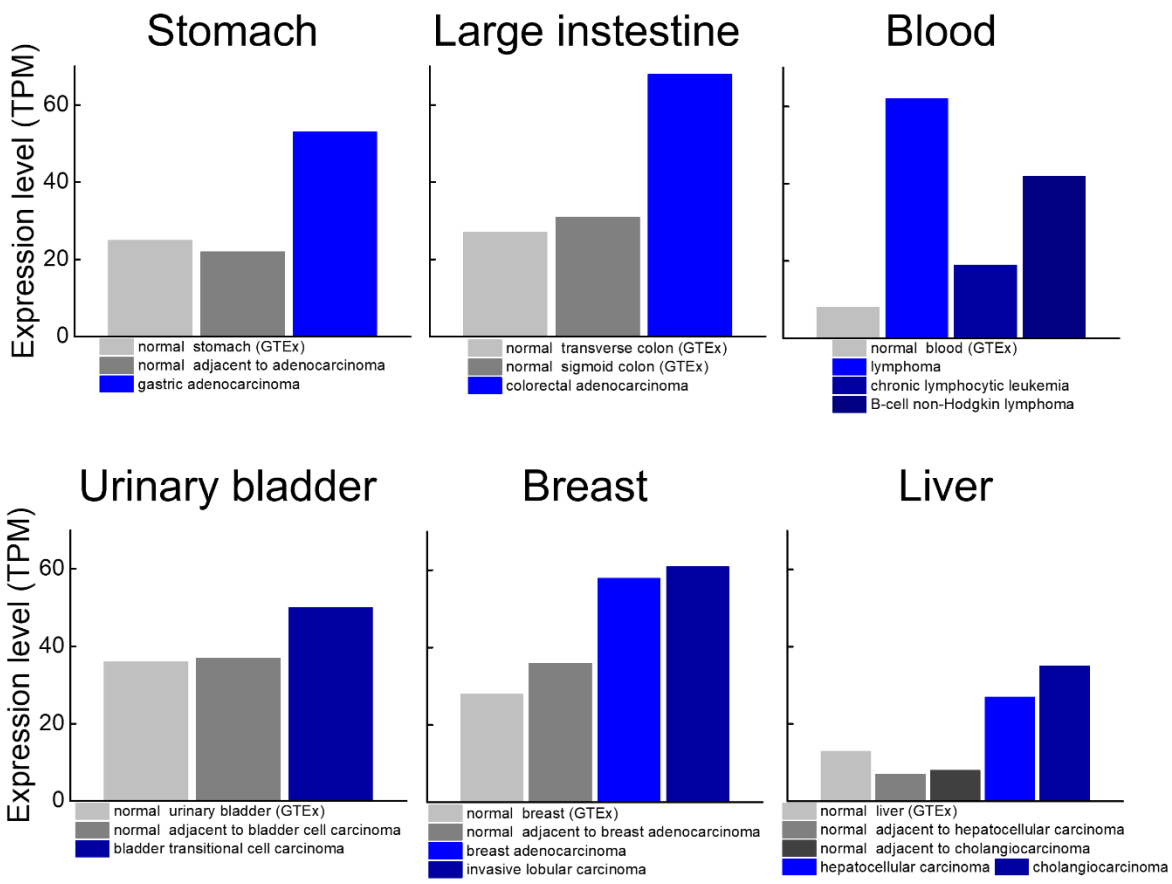

Fig. 9. hSSB1 shows elevated expression levels in various cancerous tissues. hSSB1 expression levels, displayed as TPM (transcripts per million), are shown for non-cancerous (grey shades) and cancerous (blue shades) tissues (GTEx: Genotype-Tissue Expression, data source: Expression Atlas, https://www.ebi.ac.uk/gxa/home).